



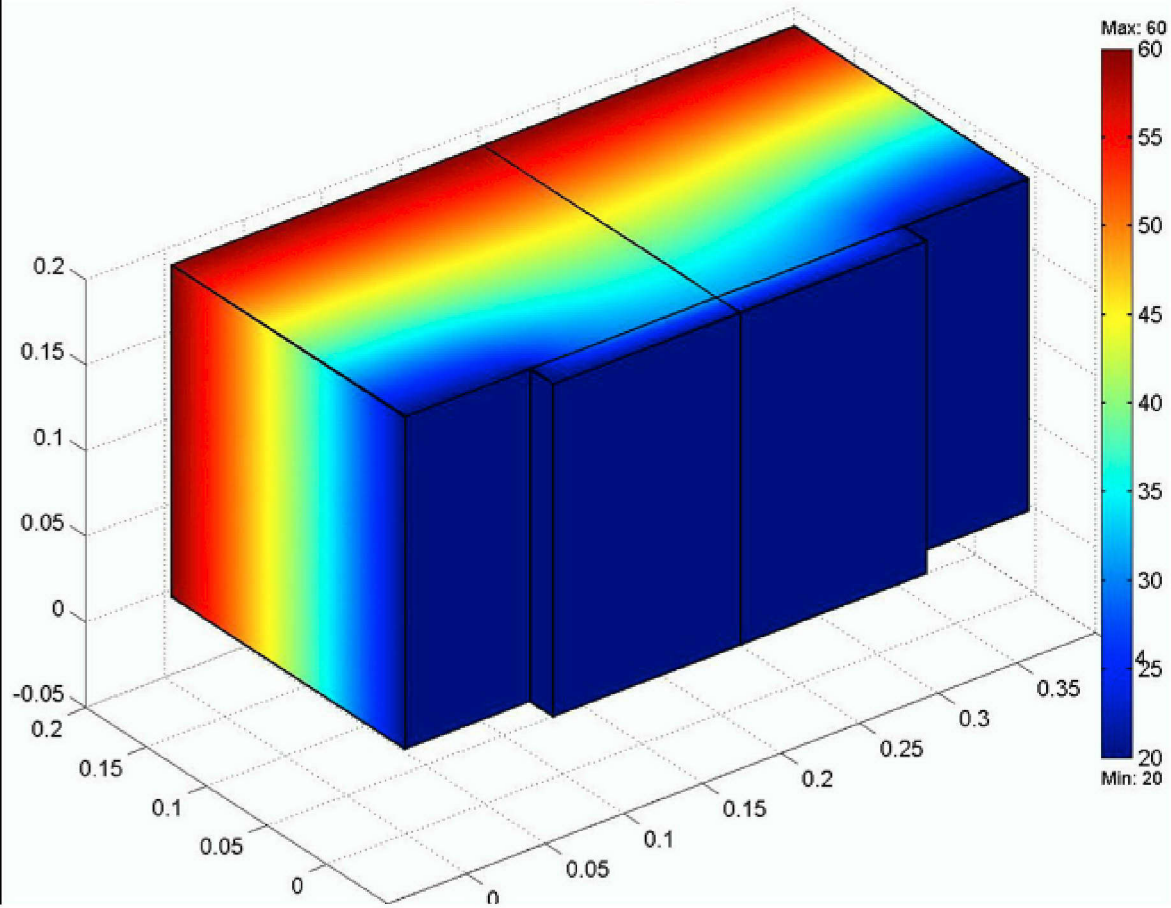
US Army Corps  
of Engineers®

Engineer Research and  
Development Center

## Hygrothermal Modeling in the Application of Fiber-Reinforced Polymers for Structural Upgrade of Unreinforced Masonry Walls

Carl A. Feickert, Mark W. Lin, Jonathan C. Trovillion,  
Ayo O. Abatan, and Justin B. Berman

September 2003





# Hygrothermal Modeling in the Application of Fiber-Reinforced Polymers for Structural Upgrade of Unreinforced Masonry Walls

Carl A. Feickert, Jonathan C. Trovillion, and Justin B. Berman

Construction Engineering Research Laboratory

PO Box 9005

*Champaign, IL 61826-9005*

Ayo O. Abatan

### **Clark Atlanta University, GA**

Mark W. Lin

## *University of Alabama, Huntsville*

## Final Report

Approved for public release; distribution is unlimited.

**ABSTRACT:** The Army maintains an aging inventory of over 143,000 structures, many of which are in urgent need of maintenance and repair. In some instances, these aging structures fail to meet prevailing seismic engineering codes. In the United States alone, 30 percent of the Army's structures use unreinforced masonry (URM) walls. As such, URM structures have inadequate plane lateral strength and are prone to failure during seismic events. Upgrading these structures to meet existing seismic codes often requires the use of new materials and systems such as fiber-reinforced-polymer (FRP) composites. The versatility and resilience of such advanced composites make them ideal candidate materials for reducing the cost of seismic rehabilitation of DOD facilities. Though many studies have demonstrated the effectiveness of FRP reinforcements as structural upgrades for masonry walls, little has been done to explain their impact on the building envelope. This study was undertaken to discover and define the combination of building envelope and hygrothermal conditions that might result in vapor liquefaction at the ceramic-epoxy interface, and subsequently debond or delaminate the applique. This research developed fundamental models and associated material parameters to predict thermal and moisture transport across dissimilar building materials—specifically FRP composite appliques to concrete masonry units (CMUs)—used for seismic upgrades.

**DISCLAIMER:** The contents of this report are not to be used for advertising, publication, or promotional purposes. Citation of trade names does not constitute an official endorsement or approval of the use of such commercial products. All product names and trademarks cited are the property of their respective owners. The findings of this report are not to be construed as an official Department of the Army position unless so designated by other authorized documents.

DESTROY THIS REPORT WHEN IT IS NO LONGER NEEDED. DO NOT RETURN IT TO THE ORIGINATOR.

# Contents

<b>List of Figures and Tables .....</b>	<b>iv</b>
<b>Conversion Factors .....</b>	<b>vi</b>
<b>Preface.....</b>	<b>vii</b>
<b>1 Introduction .....</b>	<b>1</b>
1.1 Background.....	1
1.2 Objective.....	3
1.3 Approach.....	3
1.4 Mode of Technology Transfer .....	3
<b>2 Moisture Infiltration of Porous Structures.....</b>	<b>5</b>
2.1 Moisture and Thermal Transport Equations .....	7
2.2 Interfacial Conditions of Continuity.....	8
2.3 Thermal Transport Equations .....	9
2.4 Some Particulars for $D_\theta(\theta)$ in Cementitious Materials .....	10
2.5 Diffusion of Moisture in Polymers .....	11
<b>3 Computer Modeling and Simulation .....</b>	<b>15</b>
3.1 Numerical Solutions and Finite Element Implementation.....	17
3.2 Numerical Solutions for Moisture, Total FRP-CMU Coverage.....	23
3.3 Numerical Solutions for Moisture, Partial FRP-CMU Coverage .....	25
<b>4 Coupled Moisture, Temperature, and Structural Analysis.....</b>	<b>31</b>
<b>5 Conclusions.....</b>	<b>41</b>
<b>References.....</b>	<b>44</b>
<b>Appendix A: FRP-CMU Material Parameters .....</b>	<b>47</b>
<b>Report Documentation Page .....</b>	<b>56</b>

# List of Figures and Tables

## Figures

1	A typical sorption-desorption isotherm for a porous cement based material, defining the hygroscopic range and maximal moisture content beyond 98% RH .....	6
2	Diffusion coefficient variation with moisture content, for several common porous building materials (van Zijl 1999) .....	10
3	Test section of a wall (3a) constructed from CMUs, along with an individual CMU's dimensions. The 2 mm of FRP composite thickness (3b), has been exaggerated for clarity at this scale .....	16
4	3D model of the FRP reinforced concrete block: (a) schematic diagram and (b) FE model mesh (Dimensions are unitless, meant to indicate proportion only).....	18
5	Reduced 2D model of the original 3D problem used for analysis of thermal and moisture transfer. (5a) depicts lateral, interior and exterior boundary conditions; (5b) represents corresponding FE model mesh .....	19
6	1D steady-state moisture transport problem, humidity profile, with FRP totally covering the CMU; the interior FRP surface is constrained to 50% RH and 20 °C, while the exterior surface RH is held at 97% RH with the temperature permitted to vary from 10 to 60 °C .....	24
7	1D steady-state moisture transport problem, total moisture density $\theta$ profile, with FRP totally covering the CMU; the interior FRP surface is constrained to 50% RH and 20 °C, while the exterior surface RH is held at 97% RH with the temperature permitted to vary from 10 to 60 °C.....	24
8	2D steady-state moisture transport problem, humidity profile, with FRP partially covering (~60%) the CMU; data taken from the (Y-Z) symmetry plane; the interior FRP surface is constrained to 50% RH and 20 °C; while exterior surface RH is held at 97% RH with the temperature permitted to vary from 10 to 60 °C .....	27
9	2D steady-state moisture transport problem, total moisture density $\theta$ profile, with FRP partially (~60%) covering the CMU; data taken from the (Y-Z) symmetry plane; the interior FRP surface is constrained to 50% RH and 20 °C, while the exterior surface RH is held at 97% RH with the temperature permitted to vary from 10 to 60 °C .....	27
10	2D steady-state moisture transport problem, depicting total moisture flux profile (within the X-Y plane), and FRP partially (~60%) covering the CMU; this chart delineates evacuation routes available to moisture that might otherwise be trapped behind the CMU-FRP interface; the interior FRP surface is constrained to 50% RH and 20 °C; the exterior surface RH is held at 97% RH with a temperature of order 20 °C .....	28

11	10, with the corresponding X-Y humidity profile superimposed. Note that the moisture flux appears to be normal to the surfaces of constant humidity, which is an expected result given that the flux, $q$ , scales proportional to $\nabla\theta$ , (see Equation 1).....	28
12	FRP-CMU thermal profile, with FRP partially (~60%) covering the CMU; data taken from the (Y-Z) symmetry plane; the interior FRP surface constrained to 50% RH and 20 °C; exterior surface RH is held at 97% RH with the temperature permitted to vary from 10 to 60 °C.....	29
13	Schematic of displacement boundary conditions.....	34
14	Temperature contour of the concrete slab partially covered with an FRP laminate (°C) .....	35
15	Relative humidity contour of the concrete slab partially covered with an FRP laminate.....	35
16	$\tau_{xy}$ shear stress contour in the concrete slab (Pa) .....	37
17	$\tau_{xy}$ shear stress contour in the FRP laminate (Pa) .....	37
18	Displacement $u_x$ contour depicted on the deformed geometry of the model on the x-y plane (m) .....	38
19	$\tau_{yz}$ shear stress contour in the concrete slab (Pa) .....	38
20	$\tau_{yz}$ shear stress contour in the FRP laminate (Pa) .....	39

## Tables

1	Some experimental values of fitting parameters used to define $D_\theta$ in Equation 5, for several listed polymeric materials .....	14
2	Material Properties for concrete and FRP.....	33

## Conversion Factors

Non-SI\* units of measurement used in this report can be converted to SI units as follows:

Multiply	By	To Obtain
Acres	4,046.873	square meters
cubic feet	0.02831685	cubic meters
cubic inches	0.00001638706	cubic meters
degrees (angle)	0.01745329	radians
degrees Fahrenheit	(5/9) x (°F – 32)	degrees Celsius
degrees Fahrenheit	(5/9) x (°F – 32) + 273.15.	kelvins
Feet	0.3048	meters
gallons (U.S. liquid)	0.003785412	cubic meters
horsepower (550 ft-lb force per second)	745.6999	watts
Inches	0.0254	meters
kips per square foot	47.88026	kilopascals
kips per square inch	6.894757	megapascals
miles (U.S. statute)	1.609347	kilometers
pounds (force)	4.448222	newtons
pounds (force) per square inch	0.006894757	megapascals
pounds (mass)	0.4535924	kilograms
square feet	0.09290304	square meters
square miles	2,589,998	square meters
tons (force)	8,896.443	newtons
tons (2,000 pounds, mass)	907.1847	kilograms
Yards	0.9144	meters

\*Système International d'Unités ("International System of Measurement"), commonly known as the "metric system."

## Preface

This research was conducted for the Directorate of Military Programs, Headquarters, U.S. Army Corps of Engineers (HQUSACE) under Project AT23, Basic Research in Military Construction, "Military Facility Engineering Technology"; Work Unit 007AV5, "Long-Term Performance Modeling of Structural Composite Elements." The technical monitor was Dr. Paul A. Howdyshell, CEERD-CV-ZT.

This research project was originally initiated and executed by the Materials and Structures Branch (CF-M), Construction Engineering Research Laboratory (CERL), with Dr. Justin Berman as the Principal Investigator, and Martin Savoie as the Chief, CEERD-CF-M. Dr. Berman became the Chief of the Applied and Military Engineering Branch of the Cold Regions Research and Engineering Laboratory (CRREL) in November 2002. This work was subsequently performed by the Energy and Utilities Branch (CF-E) of the Facilities Division, CERL. A portion of this work was performed under contract DACA42-01-C-0028 to Dr. Ayo Abatan, Clark Atlanta University (CAU). The authors wish to acknowledge the invaluable help provided by the ERDC-CERL library staff, especially Ms. Patricia Lacey, whose steadfast attention to detail and persistent pursuit of literature references made this research effort both productive and possible. The Principal Investigator was Dr. Carl Feickert. Dr. Thomas Hartranft is Chief, CEERD-CF-E, and L. Michael Golish is Chief, CEERD-CF. The Acting Technical Director of the Facility Acquisition and Revitalization business area is Dr. Paul A. Howdyshell, CEERD-CV-ZT. The Director of CERL is Dr. Alan W. Moore.

CERL is an element of the U.S. Army Engineer Research and Development Center (ERDC), U.S. Army Corps of Engineers. The Commander and Executive Director of ERDC is COL John Morris III, EN and the Director of ERDC is Dr. James R. Houston.



# 1 Introduction

## Background

The Army maintains an aging inventory of over 143,000 structures, many of which are in urgent need of maintenance and repair. In some instances, these aging structures fail to meet prevailing seismic engineering codes. In the United States alone, 30 percent of the Army's structures are constructed with unreinforced masonry (URM) walls. URM structures have an inadequate plane lateral strength and are consequently prone to failure when subjected to natural hazards (e.g., seismic events).

Upgrading these structures to meet existing seismic codes often requires the use of new materials and systems such as fiber-reinforced-polymer (FRP) composites. FRP and other advanced composite materials offer many advantages over more conventional building materials. Their high specific stiffness and specific strength properties, coupled with their intrinsic corrosion resistance and ease of application make them ideal for incorporation into many existing lightweight composite structural elements. They can conform to non-planar surfaces, can be cut and applied in various forms, and if applied properly, need not cover the entire surface of the URM wall. When bonded to URM walls, they can greatly enhance the ductility of the wall. Moreover, many of these materials are "environmentally friendly." They consume less energy during fabrication than do traditional materials, and can be applied *in situ*. These features combine to reduce construction and shipping costs, which becomes particularly evident (and desirable) when materials are required in remote construction locations. In summary, the versatility and resilience of advanced composites make them ideal candidate materials for reducing the cost of maintenance and for seismic rehabilitation of DOD facilities.

Though many studies have demonstrated the effectiveness of FRP reinforcements as structural upgrades for masonry walls (Al-Chaar and Hassan 2002; Marshall, et al. 1999; Saadatmanesh 1997; Kim and Lee 1998; Sakata 1983; Anand and Gandhi 1983), little has been done to explain their impact on the building envelope. A crucial feature in the use of any composite applique is the ability of the composite to remain in intimate structural contact with the supporting member undergoing retrofit. Detailed knowledge of the physical parameters of

both applique and substrate, compounded with any environmental factors, will collectively define the parameter space of application. It is of particular interest to model the moisture migration in an FRP upgraded URM wall structure since the adhesive interface between the FRP laminate and the host masonry can be susceptible to moisture entrapment. Moisture entrapment can lead to a reduced load transfer at the FRP/masonry interface or result in premature FRP debonding. Thus, the mechanical durability of the composite-substrate interface and attendant viscoelastic sensitivities to moisture and temperature fluctuations can be the defining parameters for many applications. This matter is further complicated by the fact that composites may be exposed to many different harsh external environments ranging from extremely cold climates (e.g., Fairbanks, AK) to warm, humid climates (e.g., Key West, FL).

A decade of field data and laboratory research has continued to justify and champion the use of FRP upgrades for URM when executed in a consistent and conscientious manner by trained professionals. However, research has shown that the true kinetics of moisture absorption (FRP/URM) under freeze-thaw exposure in aqueous solutions is not yet well understood. The current body of literature does not explain the presence of microcrack and fiber-matrix debond related degradation and possible mass dislocation under these conditions (Rivera and Karbhari 2002). As such, long-term predictions made using models based on short-term phenomena of several studies may lead to an overly optimistic deployment-parameter envelope.

During the same period, computer technology made significant strides. The cost of computer simulations declined exponentially with the appearance of inexpensive memory and faster clock speeds. User-friendly software has kept pace with these rapid hardware innovations, particularly those employing Finite Element Codes. At the same time, a branch of research known as "Building Physics" was begun in Northern Europe and Canada. Careful experiments on common building materials using innovative measurement techniques generated research data that explained how temperature and moisture commingled in a collective migration through test specimens.

The coincidence of these events has made computer simulation a valuable research tool to help resolve the role of hygrothermal effects in the application of FRP composites to the building envelope. This study was undertaken to discover and define the combination of building envelope and hygrothermal conditions that might result in vapor liquefaction at the ceramic-FRP interface, and subsequent debonding of the applique.

## Objective

The objective of this research was to develop fundamental models and associated material parameters to predict thermal and moisture transport across dissimilar building materials—specifically FRP composites appliques to concrete masonry units (CMUs)—used for seismic upgrades.

## Approach

This work involved:

1. Developing a detailed description of the physical mechanisms responsible for (non-saturated) moisture migration through porous materials, and of the related role of temperature in this transport process.
1. Performing a detailed literature review to obtain the physical parameters that appear in the coupled hygrothermal equations (which have both sensitivity to moisture and temperature), and details of how these parameters are measured.
2. Modification of commercial computer software to solve the coupled set of moisture and thermal differential equations derived in the previous steps.
3. Using these derived results to provide modified strain boundary conditions as initial data required in standard stress-strain analyses of mechanical systems.
4. Interpreting the hygrothermal and mechanical results to provide conclusions and recommendations for the deployment of FRP-CMU appliques in overall building envelope design.

## Mode of Technology Transfer

It is anticipated that the modeling effort developed in this work will be used in conjunction with mechanical strain models to improve the placement and performance of FRP composites, and ultimately, to improve overall building envelope design. Immediate plans are to incorporate the fundamental models and results from this basic research project into seismic upgrade AT41 projects, including “Accelerated Performance and Weathering of Structural Repair and Upgrade Composites,” and “Seismic Rehabilitation of URM Walls.” The results of this work will continue to be disseminated through scientific and trade literature. Current journal articles and professional presentations resulting from this work unit are:

Lin, M.W., M. Kahbahda, J. Berman, C.A. Feickert, and A.O. Abatan. 2002. “Nonlinear Finite Element Modeling of Moisture Migration in a Masonry Structure with FRP Upgrade,” ISBN 0864912323, presented at CanCNSM, Vancouver, B.C., 19-23 June 2002.

A. Abatan, M. Lin, et al., "Durability of Fiber Reinforced Polymer Composites Under Varying Environmental Behavior," The 4th Canadian International Composites Conference, CANCOM 2003, 19-22 August 2003, Ottawa, Canada.

This report will be made accessible through the World Wide Web (WWW) at URL:

<http://www.cecer.army.mil>

## 2 Moisture Infiltration of Porous Structures

During the past several decades, the area of building physics research has developed into a mature multifaceted discipline particularly in the countries of Northern Europe. The discipline owes its rigorous heritage to the formal investigations of earlier researchers like Philip and De Vries (1957), and Luikov (1975), who applied thermodynamics and Navier-Stokes considerations to the detailed theory of heat and mass transfer in porous materials. Such results have enabled engineers to perform detailed modeling calculations on common building materials and thereby to more accurately assess their suitability to a given moisture and temperature regime.

Many of the appliques and substrates in particular tend to be porous, and to have material properties that are particularly sensitive to ambient humidity (moisture) and temperature. Porous materials tend to absorb moisture from the surrounding moist air. This uptake of water vapor (moisture) is referred to as “sorption,” which continues until a state of equilibrium is reached. The moisture content of the material at this state is referred to as the “equilibrium moisture content,” characterized by the parameter  $\theta$ . The moisture content,  $\theta$ , is typically measured in units of mass per unit volume of the dry material ( $\text{kg}/\text{m}^3$ , the unit used in this work),  $u$  the mass of adsorbed water per mass of the dry material ( $\text{kg}/\text{kg}$ ), or sometimes volume of water per volume of dry material ( $\text{m}^3/\text{m}^3$ ). The moisture content,  $\theta$ , is related to these other measures by multiplying them by the (dry) density of the porous material or the density of water, respectively.

Because of this sorptive property, there exists an important defining relationship between the vapor pressure of water, or relative humidity (RH) of the ambient air, and the *equilibrium* moisture content within the material. The essence of this correlation is described by a curve called the “sorption isotherm.” Figure 1 shows a typical sorption isotherm, characteristic of a large class of porous building materials (Valen 1998; van Zijl 1999; Janz 1997). The curve relates the moisture content  $\theta$ , to ambient humidity  $h$ , and has a characteristic sigmoid shape, with the slope of the linear region defining the moisture capacity ( $\xi$ ) of the material. At constant relative humidity of the surroundings, the equilibrium moisture content decreases with increasing air temperature, however the difference in moisture content is small (Valen 1998).

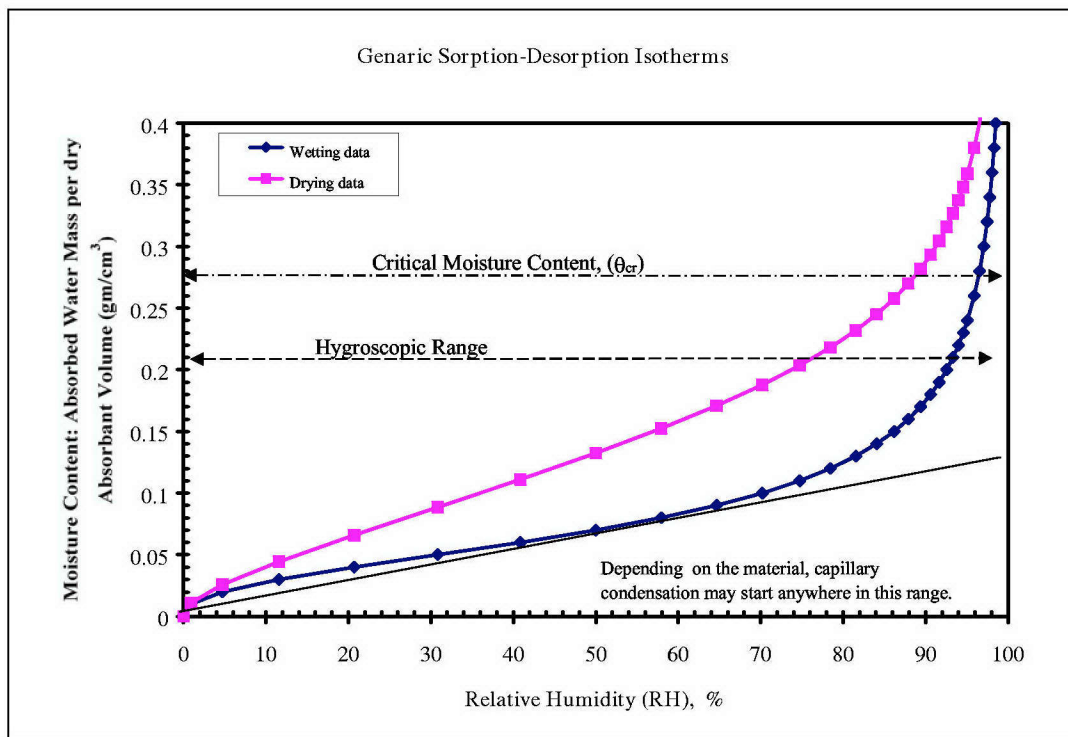


**Figure 1. A typical sorption-desorption isotherm for a porous cement based material, defining the hygroscopic range and maximal moisture content beyond 98% RH.**

The figure defines the hygroscopic range, critical moisture content, capillary and maximum moisture content of a porous material. The range of RH between 0 and 98 percent is defined as the hygroscopic range. Beyond the hygroscopic range, when the RH is higher than 98 percent, capillary moisture condensation occurs within the pores. At this stage, there is as yet no continuity of the liquid in the capillaries. This process continues until a critical moisture content,  $\theta_{cr}$  (defined as the lowest moisture content necessary to initiate contiguous moisture transport in the liquid phase), is established. Below this level, moisture is transported only in the vapor phase, even though there exists (isolated) capillary moisture condensation. In addition, because of the sponge-like feature of porous materials (i.e., the porosity is fractal), the reverse process of moisture outgassing is characterized by hysteresis, thereby ensuring a nonlinear diffusion mechanism. For the purposes of this study:

1. All moisture (liquid and vapor) is assumed to be transported within the hygroscopic range. No freezing, boiling, or melting occurs.
2. Both adsorption and desorption isotherms are single valued functions of the ambient relative humidity. Consequently, the models presented here only describe monotonic wetting or drying processes. Cyclic excursions within the hygroscopic region require a more detailed analyses and knowledge of the material properties.

## Moisture and Thermal Transport Equations

To quantify the migration process further, one applies Fick's law for moisture flux and the general continuity equations to a given media. The resulting coupled equations assume that the moisture content,  $\theta$ , is not lost through any curing mechanism, but serves (generally, along with  $T$ ) as the driving potential (i.e., state variables) for diffusion. Finally, gravitational and dynamic pressure difference (i.e., wind) effects will be considered negligible for the particular formulation given below.

$$\frac{\partial \theta}{\partial t} + \nabla \cdot \mathbf{q} = 0 \quad \text{Eq 1}$$

$$\mathbf{q} + \mathbf{D}_\theta \nabla \theta + \mathbf{D}_T \nabla T = 0$$

Here  $\mathbf{q}$  depicts the flux vector in units of (kg/m<sup>2</sup>.s) and the functions  $D_\theta$  and  $D_T$  refer to the total (liquid plus vapor) moisture diffusivity and thermal (liquid plus vapor) diffusivity, respectively. The units of  $D_\theta$  generally depend on those of  $\theta$ ; choosing  $\theta$  in units of (kg/m<sup>3</sup>) yields units of (m<sup>2</sup>/s) for  $D_\theta$ , with corresponding similar considerations for  $D_T$ .

The compactness of these equations belies considerable subtlety in their formulation (Janz 1997), and implicitly incorporates the fact that present technology cannot make a meaningfully distinction between *in situ* moisture in its liquid or vapor phases. During any water transport process, there will always exist evaporation or condensation at the water menisci. Thus, there will be a phase transformation between the vapor and liquid phases. The equations that describe each of these *separate* phase flows contain additional terms that sum to zero when the total moisture is considered, as in Equation 1 above.

Analogous formulations of Equation 1 exist depending on the details and choice of driving potential (Valen 1998), and are normally used within the hygroscopic region (0-98 percent RH). However the analytic form of Equation 1 is sufficiently general so as to be applicable to the whole region from dry material up to 100 percent humidity, provided modifications to  $D_\theta$  and  $D_T$  are made that incorporate the new hygro-thermal physics that is present when  $h > 98$  percent RH. Further, Equation 1 is implicitly formulated with the notion that all moisture transport of capillary absorption measurements occurs in liquid phase, and all moisture transport in the cup-method measurement occurs in vapor phase. In practice, it is more appropriate to use dry-cup values and adjust the liquid transport coefficients to include surface diffusion. A notable exception are plastic film coatings, where the vapor permeability itself can increase considerably

with humidity because water molecules creep between the polymer chains and thus change the polymer structure (Kuenzel et al. 2000).

In addition, it is also important to keep in mind the mathematical model for which the measured data will be used. For example, transport coefficients measured under isothermal conditions cannot automatically be used in non-isothermal models. If the moisture content  $\theta$  and the temperature  $T$  are used as state variables in the non-isothermal model, the transport coefficients will be  $D_\theta(\theta, T)$  and  $D_T(T, \theta)$  respectively. In this case, measurements must be performed at varying moisture contents and moisture *gradients*, and at different temperature levels and temperature *gradients* (Claesson 1993). In doing so, one is then able to determine the first order contributions of a general Taylor series expansion for  $D_\theta(\theta, T)$  and  $D_T(T, \theta)$ . Fortunately, for many practical instances, one may simply consider  $D_\theta = D_\theta(\theta)$ , with the  $T$  sensitivity being a higher order term. Similarly  $D_T$  is considered to have a slowly varying sensitivity to the local temperature and relative humidity.

## Interfacial Conditions of Continuity

Equations 1 are incomplete as presented; all differential equations require a set of boundary conditions for their complete solution. In most cases, these conditions are defined by some combination of relevant physics and constraining geometry. These constraints are typically developed and executed at the surfaces or boundaries of the system, which gives rise to the nomenclature. Two distinct materials that are in close contact with each other, and share a common surface with some degree of interpenetration, are said to be in “Natural Contact.” As such, the moisture content,  $\theta$ , of the two materials can have vastly different values, so will be discontinuous at the interface. However for a system that is in equilibrium at any instant, the total (entering and leaving) moisture flux perpendicular to the surface of a given volume must remain constant. Furthermore, it is an experimental fact that the vapor pressure of water (related to the relative humidity) is the same at both surfaces. For such surfaces in natural contact, the continuity of normal flux vector component (Equation 1),  $q_n$ , and the relative humidity,  $h$ , across an (A-B) interface:

$$q_n^A = q_n^B \quad \text{Eq 2}$$

$$h_A = h_B$$

provide the required set of boundary conditions for Equation 1.

## Thermal Transport Equations

The set of Equations 1 and 2, are insufficient to completely describe moisture migration through any real material system with a finite specific heat capacity,  $c$ , since such moisture transport intrinsically involves a two-phase (thermal) system. A second set of equations that describe the thermal fluxes through the individual system components (sometimes referred to as the “energy equations”) is required:

$$\rho c(\partial T / \partial t) = \nabla \cdot (k_T \nabla T) + h_v \nabla \cdot (D_T \nabla T) \quad \text{Eq 3}$$

Here:

- $\rho$  = the host material's mass density in  $\text{kg/m}^3$ , and is typically a function of the amount of moisture contained within a porous material.
- $c$  = the host material specific heat in  $\text{J/kg.K}$ , and is also a function of moisture content.
- $k_T$  = the host material thermal conductivity in  $\text{Watts/m.K}$ , and is similarly a function of moisture content.
- $h_v$  = the latent heat of evaporative phase change, in  $\text{J/kg}$ . Handbook values for water are listed as 2,500.9  $\text{kJ/kg}$  at 0  $^{\circ}\text{C}$ , and 2,256.8  $\text{kJ/kg}$  at 100  $^{\circ}\text{C}$ .

For heat and moisture transport, the traditional boundary conditions are required, in particular the continuity of normal component of thermal flux, and temperature at an interface.  $D_T$  is as defined in Equation 1 above, however a simplification is possible. Explicit calculation of  $h_v(D_T)$  using the formalism found in Appendix A clearly shows that this term is several orders of magnitude smaller than a typical  $k_T$ . However, the term has been included in Equation 3 for completeness.

Collectively, Equations 1 to 3 are sufficient to define moisture migration within the hygroscopic regions (Figure 1) for each set of materials in a masonry-FRP applique. In the most general case, these nonlinear equations must be solved iteratively with  $T$  as the connecting variable. However for the ceramic-epoxy-FRP system, the  $k_T$  of a typical CMU is at least an order of magnitude greater than that of the epoxy or FRP. This affords a great simplicity by effectively decoupling the two equations in temperature but not necessarily in time. In doing so, one is able to first solve Equation 3 and thereby prescribe the thermal field distribution for a given moisture profile,  $\theta = \theta(r, t = \text{constant})$ . The resulting thermal solution,  $T = T(r, t = \text{constant})$ , can then be used to solve for a new subsequent moisture migration resulting from the prescribed thermal field.

## Some Particulars for $D_\theta(\theta)$ in Cementitious Materials

Figure 2 shows the general features of a diffusivity curve,  $D_\theta = D_\theta(\theta)$  for several common ceramic materials. The actual details depend on specific material properties. However some generalizations are possible:

$$\log_{10}(D_\theta \text{ m}^2/\text{s}) \approx A\theta + B \text{ (dimensionless).}$$

$$\text{for: } 0.0 < \theta \text{ (kg/m}^3\text{)} \leq 250, \text{ and} \quad \text{Eq 4}$$

$$0.013 < A \text{ (m}^3/\text{kg)} \leq 0.022; -11.0 < B \leq -9.0$$

These values of A and B were summarized from van Zijl (1999) and characterize materials such as mortar, sand-lime 1, clay brick, and calcium silicate. Equation 4 provides a reasonable description of  $D_\theta$  for these materials during the sorption (wetting) phase of water uptake. During the drying phase,  $D_\theta$  is found to be typically larger by a factor of 10, and  $\log_{10}(D_\theta)$  executes a sharp increase for (drying)  $\theta$  values between  $50 > \theta \text{ (kg/m}^3\text{)} \geq 0.0$ . These features are consistent with the aforementioned hysteresis of  $\theta$ , and have been attributed by Pel (1995) to the transition from liquid to vapor-dominated moisture transport.

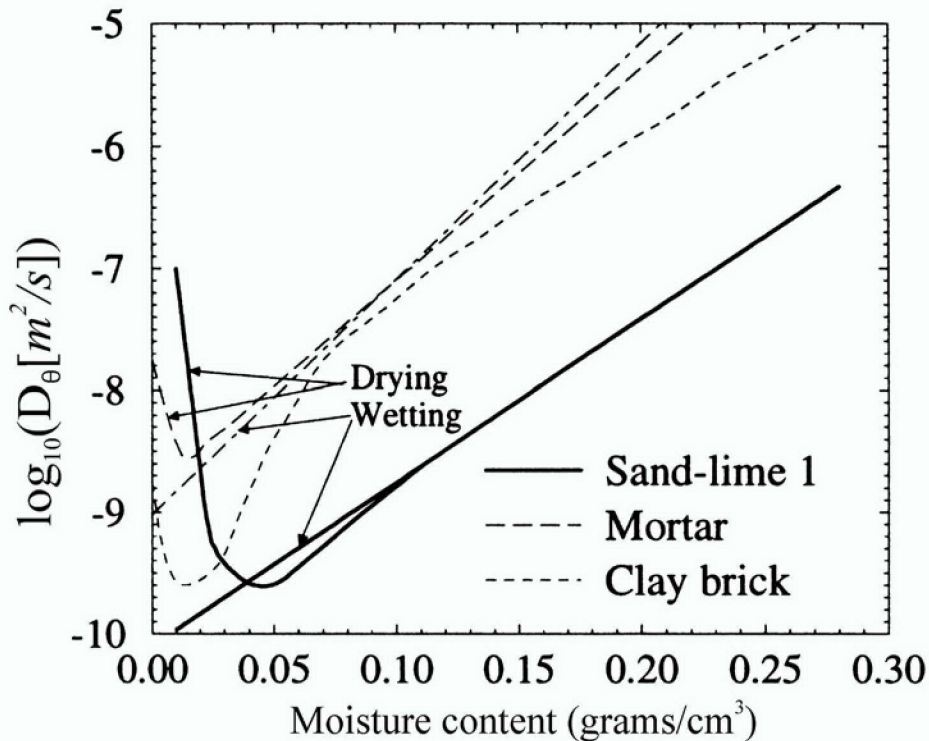


**Figure 2. Diffusion coefficient variation with moisture content, for several common porous building materials (van Zijl 1999).**

Thus while  $D_\theta$  performs a pivotal function in Equation 1, its ultimate functionality is constrained by the isothermal sorption curve (Figure 1). This is particularly relevant when the RH is changing. As the water vapor diffuses into the material according to the diffusion coefficient, it is being absorbed by the pore wall structure, according to the sorption coefficient. A material with both a high diffusivity and a high absorption coefficient will appear to retard the transport of water vapor under dynamic circumstances because the water is absorbed before it can appreciably diffuse.

In recent years, percolation theory has offered a valuable paradigm for gleaning insights into the defining physics responsible for many of these features; the review by Celia et al. (1995), is particularly helpful. In addition, the advent of new technology, such as NMR, has enabled the detailed measurements of actual in situ moisture profiles in real time experiments. These observations provide the crucial data for the sorption and desorption of moisture coefficients under a variety of environmental conditions and materials. The reader is referred to the excellent works of Pel (undated).

Finally for realistic modeling of any physical system, one must be aware of the impact that any ancillary boundary conditions can have on a set of (perceived) primary boundary conditions. This constraint can be particularly crucial for a porous system containing both invading and receding fluids (Aker 1996; Descamps 1997). Descamps has observed that water imbibition into porous building materials is a two-phase flow process in which the imbibing water displaces the air that is initially present in the pore space. Accurate non-destructive measurements of transient moisture profiles during imbibition into calcium silicate brick indicate that the air outflow boundary condition has a predominant influence on the water imbibition process. As a consequence, significant differences have been observed in the water sorption and transport coefficients derived from water imbibition experiments with free and bounded air outflow boundary conditions.

## Diffusion of Moisture in Polymers

The set of Equations (1 to 3) and the attendant diffusivity functions, defines the basic diffusion mechanisms for moisture migration through the masonry portion of the masonry-FRP applique. The same equation set exists for each region, but with a different  $D_\theta$  and  $D_T$  functionality and attendant sorption curves. In particular, the literature concerning the effects of fluids on polymeric composites has increased dramatically in recent years, in part due to the immense variety of materials and circumstances associated with these compounds. Polymers are

highly complex materials that vary in structure and physico-chemical properties. FRP composites adjoin an assortment of fibers with intricate fiber/matrix inter-phases and bondings, further complicating the resultant composite. The complexity is further confounded by the sorption of many different fluids, each with its own unique interaction between the polymer, fiber, and interface within the composite (Weitsman 1995).

The primary issues associated with the mechanical performance of FRP composites in the presence of fluids, concerns their dimensional stability, strength, fatigue response, and impact resistance above and below the glass transition temperature,  $T_g$ . To a large degree, these issues are still only partially understood, even in the absence of fluids. Polymers are somewhat porous, but share many of the diffusion and sorption considerations of their ceramic counterparts, including hysteresis. However unlike the typical (cured) ceramic, polymeric volume changes can be quite sensitive to the infusion of a variety of penetrant liquids. Typical volume strains of 2 percent are common for comparable water weight-percent uptake in a sorptive polymer. Finally, the application geometry of the polymer can play a key role in the effective diffusion coefficient, and increases of several orders of magnitude have been reported for polymeric films in going from a dry to moist state (Valen 1998).

To quantify the many features found in the typical polymer system undergoing fluid uptake (i.e., moisture), Lefebvre et al. (1989) set forth a model for the non-linear diffusion coefficient formulated on a methodology to relate the diffusion coefficient of small penetrant molecules to temperature, strain, and penetrant concentration. The approach is based on well known free volume theories of Doolittle and others (Ferry 1980), and assumes that the transport kinetics are governed by the constant redistribution of the free volume, caused by the segmental motions of the polymeric chains. In essence, this strain induced volume fluctuation mimics a pumping action that augments the normal diffusion process, which requires the penetrant molecule to surmount an energy barrier related to the fluctuating pore size. Their expression for the diffusion coefficient,  $D_\theta$  below the glass transition temperature  $T_g$ , is:

$$D_\theta = D_o \exp(-\Delta H/RT) \exp(A/B), \quad \text{Eq 5}$$

in which:

$$A = (\beta_D/f_o)(\varepsilon + \gamma\theta^N), \text{ and } B = (f_o + \varepsilon + \gamma\theta^N)$$

where:

- $f_0$  = the fractional free volume of the polymer, equal to the void volume divided by the specific volume
- $\epsilon$  = volume dilatation of the free volume due to external loads
- $\theta$  = the penetrant concentration, in this case moisture
- $\gamma$  = the volumetric coefficient of swelling, as the result of the penetrant adsorption
- $N$  = an adjustable parameter related to the non-zero volume change occurring during moisture uptake
- $\beta_D$  = a numerical parameter inversely related to the critical pore size, and  $R$  is the gas constant
- $\Delta H$  = an activation energy related to the effective potential barrier that must be surmounted by the penetrant molecule to percolate through the critical pore size
- $T$  = the absolute thermodynamic temperature, measured in degrees Kelvin
- $D_0$  = the diffusion coefficient in the reference state.

Equation 5 indicates that the free volume continues to govern the effect of stress and swelling below the glass transition temperature,  $T_g$ , where the fractional volume is much less temperature dependent. Below  $T_g$ , this metastable (super-cooled) state causes the free volume to collapse slowly with time until an equilibrium is reached. The phenomena is known as physical aging. Any successful diffusion modeling in the glassy range must incorporate this important effect. The implication is that these forces act primarily on very local volumetric properties such as the critical void size.

By contrast, temperature appears to affect motions over larger volumes encompassing cooperative segmental motions. The Arrhenius temperature dependence shown in Equation 5 has been observed experimentally (Comyn 1985) in numerous penetrant-polymer systems below  $T_g$ . Further, the Arrhenius form may also be used above  $T_g$ , with an activation energy ( $\Delta H$ ) differing from that below  $T_g$ , which accounts for the abrupt change in the temperature dependence at the glass transition. Lefebvre et al. (1989) proceed by explaining that, for temperatures above  $T_g$ , the  $\epsilon$  terms in A and B of Equation 5 acquire an additional temperature sensitivity proportional to  $(T - T_g)$ . The applicability of the Arrhenius form is based in thermodynamic phase transitions and is further justified on the basis of the analytical suppleness of the actual physical data.

In polymeric materials, Equation 5 affords an efficient parameterization of  $D_0$  in terms of parameters with a readily identifiable physical interpretation. As in the case of ceramics, the most reliable values for these parameters are rendered from actual experimental data. Table 1 (Lefebvre et al. 1989) lists some representative values for  $T > T_g$ .

**Table 1. Some experimental values of fitting parameters used to define  $D_\theta$  in Equation 5, for several listed polymeric materials.**

Fitting- Parameter	Ethylbenzene- Polystyrene	Toluene- Polystyrene	Toluene- Polyvinylacetate
$\beta_D/f_0$	17.9	16.4	8.8
$f_0$	0.074	0.014	0.319
$T_g$ (C°)	80	88	50.3
$N$	0.61	0.90	0.91
$\gamma$	0.48	0.51	2.10
$\text{Log}_{10}(D_0[\text{m}^2/\text{s}])$	-24.3	-24.6	-15.5

However, to demonstrate the predictive capability of their model, this work compared these experimental fitting parameters with the expected constants derivable from the model's rudimentary beginnings in Wells-Landel-Ferry theory (Ferry 1980). The values obtained for  $\beta_D/f_0$ ,  $D_0$  and  $T_g$  were in reasonable accord with empirical data, and found to be independent of the nature of the solvent. Some values for the enthalpic activation energy,  $\Delta H$ , derived from the literature are: 21.8 kJ/mol for Vinyl Ester water diffusion, 69.74 kJ/mol for Epoxy resin water diffusion, and 33.23 kJ/mol for the diffusion of water in Isopolyester (Chin et al. 1999).

### 3 Computer Modeling and Simulation

The typical unreinforced masonry wall requiring an FRP upgrade is located on the exterior surface of a building, and is a load-bearing structure of the building envelope. Masonry walls located within the interior may also require some reinforcement against seismic events, but typically are not load bearing. This study assumed that the exterior wall is constructed of a single course of CMUs without external brick facing. As such, the large majority of FRP appliques will be applied to the interior surface, where the environmental conditions of moisture and humidity are more stable and fluctuations less extreme. If the interior is kept within a comfortable range for (say) office environments (30 to 60 percent RH, and 72 to 78 °F), then common architectural and construction guidance indicates that moisture will flow towards the cooler and dryer surface. Furthermore, laboratory studies have shown that, for the sake of both economy and mechanical response, FRP reinforcement in the form of fabric strips is preferable to fabric that covers the whole surface of masonry walls (Triantafillou 1998; Rivera and Karbhari 2003).

Drawing on these facts, an initial simulation modeling effort was made using a wall built from CMU. Figure 3 shows a test section of such a wall along with the dimensions (in mm) of the individual CMUs. The grid structure that overlays the individual CMU (viewed here from the vertical) is indicative of the mesh development required for a finite element calculation. Note that, in this figure, the FRP-applique appears to cover the entire interior surface of the CMU when installed in the traditional vertical position. Since total coverage of the wall's surface is not recommended, for simulation a coverage of about 60 percent—an extreme upper limit of FRP usage—will be used.

Figure 3b shows an important feature of a typical CMU. The CMU has large empty bays (voids) that can readily communicate with the surrounding internal thermal and moisture environment from above and below. In actual usage, these internal voids can (and do) have long indirect paths that have contact with some unknown combination of interior and exterior air conditions. Given the requirement of well defined boundary conditions for the solution of the combined Equation set 1 to 3 above, this work considers a very restrictive set of thermal, moisture, and material thickness.

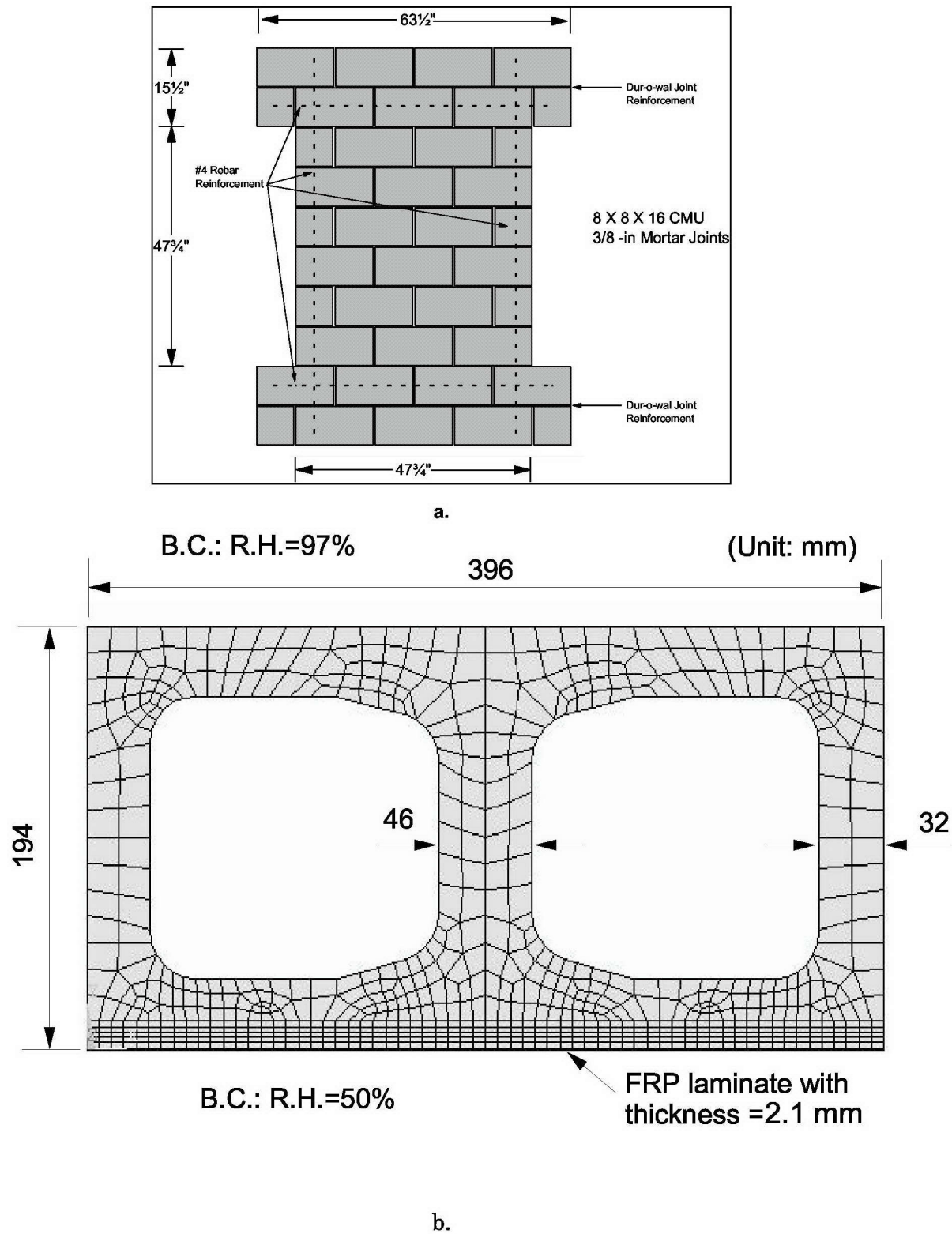


Figure 3. Test section of a wall (Figure 3a) constructed from CMUs, along with an individual CMU's dimensions. The 2 mm of FRP composite thickness (Figure 3b), has been exaggerated for clarity at this scale.

Thus, for simulation purposes, the ~36 mm of solid CMU portion nearest the FRP applique, will be considered as the defining relevant thickness of concrete, and a corresponding FRP thickness of ~2.1 mm. Results derived from these simulations must be viewed as somewhat extreme so that actual conditions of moisture and temperature gradients will be less severe.

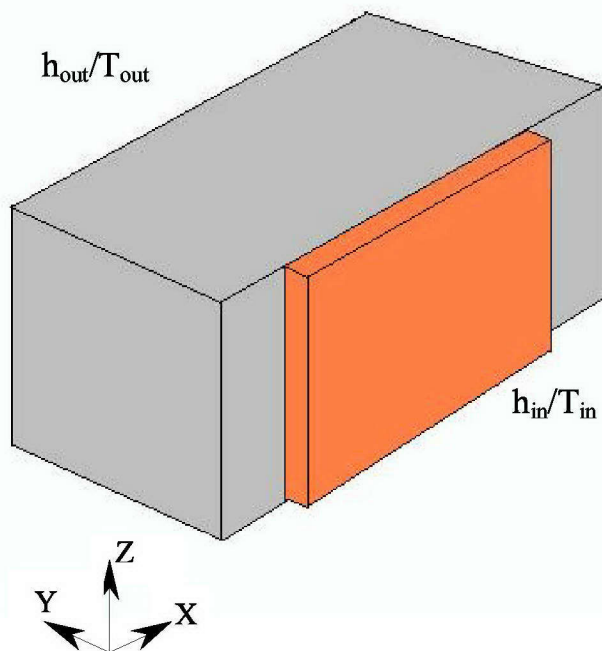
The final computational simulation is then reduced to that of modeling a single layer of *solid* CMU in natural contact with an FRP applique, that:

3. Is approximately 0.1 to 0.066 the thickness of the CMU base (Figure 4a).
4. Has the initial interior surface constrained to a hygrothermal environmental range of 30 to 60 percent RH, and 72 to 78 °F, with an exterior surface where the ambient outside humidity and temperature are free parameters,  $h_{out}$  /  $T_{out}$ , respectively (Figure 5a).
5. Has a 60 percent lateral surface coverage, of FRP applique.
6. Is surrounded by repeating and identical CMU-FRP units in the “x” and “z” direction of Figure 4a. This is also known as a “periodic boundary condition,” therefore the only thermal and moisture flux is in the “X-Y” direction. An actual three-dimensional model is needed for combined hygrothermal-mechanical analysis (Figure 4b). However under the consideration of these boundary conditions, the mass and heat transport problem can be reduced to a two-dimensional model, subject to combined temperature and moisture gradients.

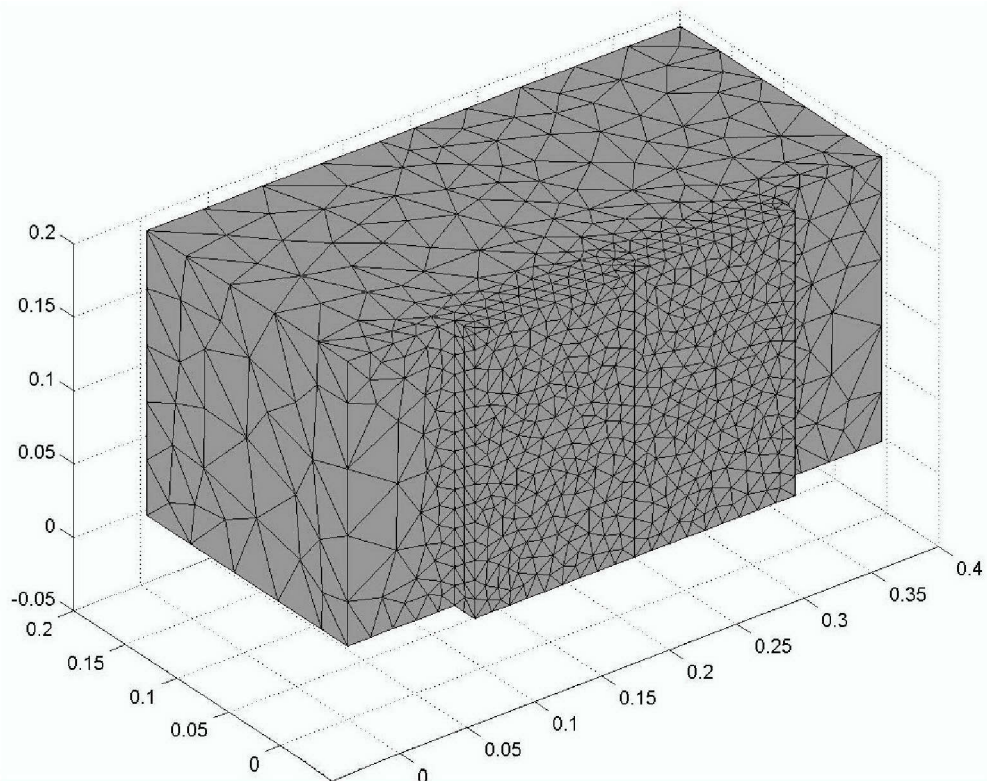
Apart from the symmetry, this is required to reduce the scale of numerical computation and the anticipated time-consuming nonlinear numerical procedures. See Figure 5a, for details and the subsequent reduction of the 3D model to the corresponding 2D analog. No attempt is made to account for or to differentiate the mortar joints connecting the individual CMU-FRP units found in a traditional layered wall.

## Numerical Solutions and Finite Element Implementation

Given the geometry and the boundary conditions required for modeling the structures in Figure 4, one can now attempt to unravel Equation set 1 to 3 for a solution. General analytic solutions involving this set of coupled, nonlinear differential equations are not possible, even for restricted 1D and 2D geometry. The problem is further confounded by the use of actual physical data (Appendix A) that is functionally dependent on the field variables of moisture,  $\theta$ , and temperature,  $T$ , and any subsequent structural analysis are by their nature three-dimensional problems.

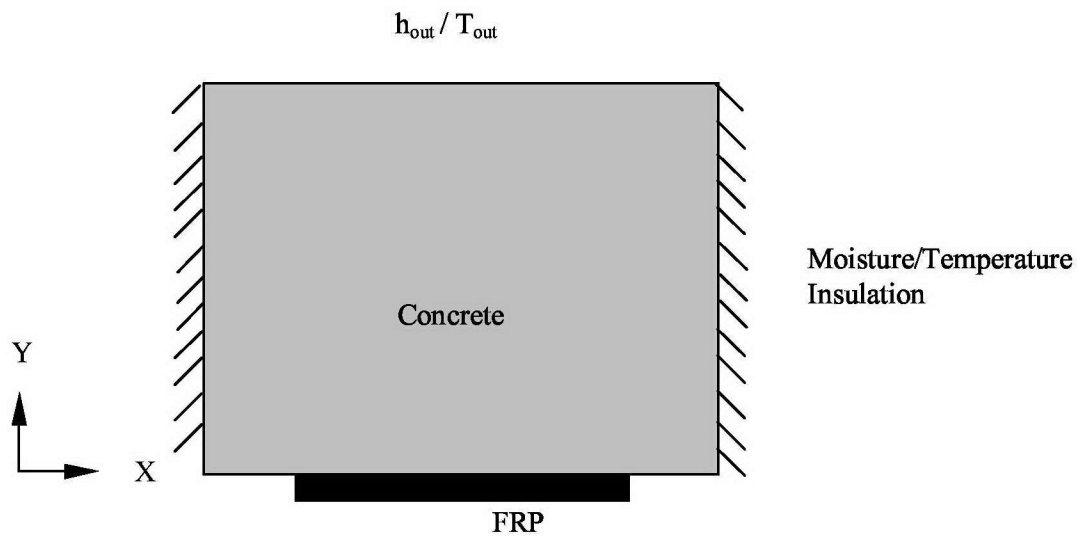


a.

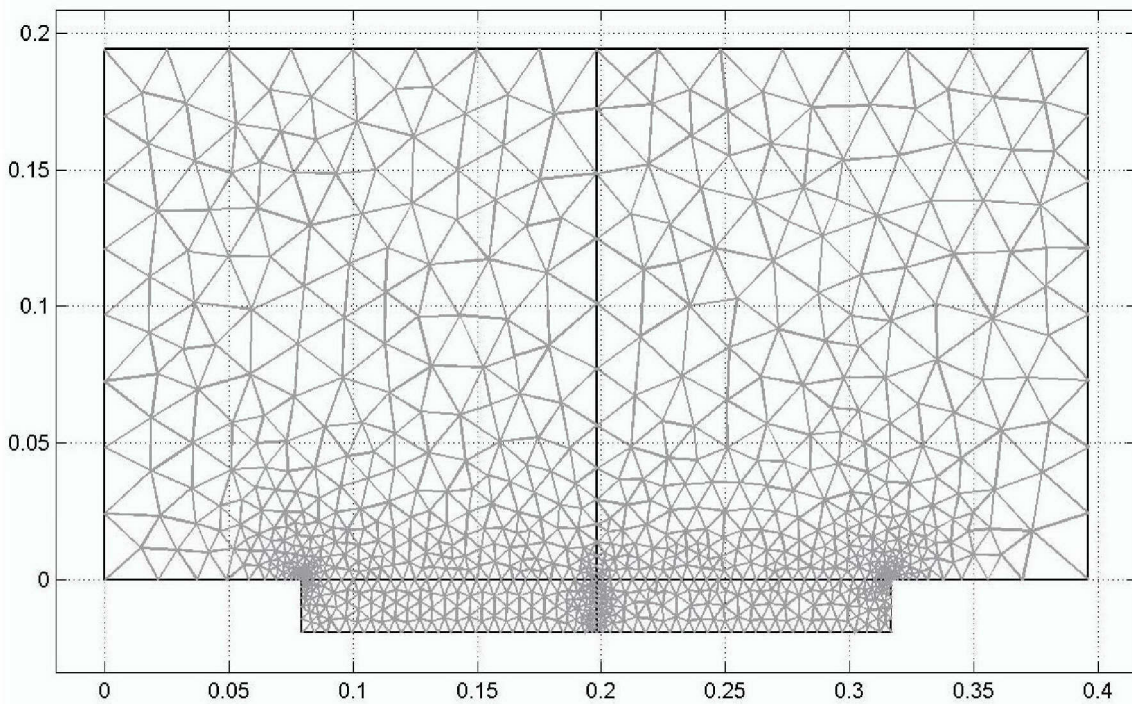


b.

**Figure 4.** 3D model of the FRP reinforced concrete block: (a) schematic diagram and (b) FE model mesh (Dimensions are unitless, meant to indicate proportion only).



a.



b.

**Figure 5. Reduced 2D model of the original 3D problem used for analysis of thermal and moisture transfer. Figure (5a) depicts lateral, interior and exterior boundary conditions; (5b) represents corresponding FE model mesh.**

Fortunately, this set of equations is responsive to general numerical analyses and solution, in particular that of the finite element method. The finite element numerical method provides great flexibility for complex model geometry and allows for parametric studies of various FRP reinforcement arrangements, which would be very difficult if not impossible using traditional theoretical analysis. In addition, the actual level of numerical modeling effort required for the detailed solution of these equations, and their attendant boundary conditions, is non-trivial. Numerical modeling services for this report were obtained through a contractual agreement between ERDC-CERL and Clark Atlanta University.<sup>11</sup>

A number of finite element packages are commercially available. This work used the ANSYS commercial package in some of the early preliminary analysis. However, the ANSYS package does not have the capability of performing coupled hygrothermal-mechanical analysis. (In fact, no commercial finite element software packages have this capability.) To implement the finite element analysis procedure, the FEMLAB finite element analysis software was chosen for the development of the coupled hygrothermal-mechanical analysis procedure. The FEMLAB software is built on the MATLAB mathematical tool using matrix operation. The program is primarily designed for solving differential equations using the finite element method. The FEMLAB finite element package allows users to modify the predefined finite element formulation and to input any type of partial differential equations to be solved in a defined geometry. The coefficients of the equations generally can be functions of independent and dependent variables.

Replacing the moisture variable with its equivalent representation in terms of humidity,  $h$ , yields the Galerkin finite element formulation of the coupled humidity and heat transport equations:

$$\int_V \left\{ \begin{Bmatrix} \delta h \\ \delta T \end{Bmatrix} [C^*] \begin{Bmatrix} \frac{\partial h}{\partial t} \\ \frac{\partial T}{\partial t} \end{Bmatrix} + \{L\}^T \begin{Bmatrix} \delta h \\ \delta T \end{Bmatrix} \begin{Bmatrix} h \\ T \end{Bmatrix} [D^*] \{L\} \begin{Bmatrix} h \\ T \end{Bmatrix} \right\} dV = \int_S \begin{Bmatrix} \delta h \\ \delta T \end{Bmatrix} \cdot \{q^*\} dS \quad \text{Eq 6}$$

where:

- $V$  = the volume of a finite element
- $S$  = surface where the vector of humidity/heat flux is specified
- $q^*$  = boundary humidity/heat flux

<sup>11</sup> Lin, Mark W., Department of Mechanical and Aerospace Engineering, University of Alabama in Huntsville, AL 35899; The prime contractor was Department of Engineering and Chemistry, Clark Atlanta University, Atlanta, GA 30314. All inquiries concerning the numerical details of this report should be addressed to Dr. Lin, at the above address; tel: (256) 824 6325; or e mail: lin@mae.uah.edu.

$\begin{Bmatrix} \delta h \\ \delta T \end{Bmatrix}$  = the vector of an allowable virtual humidity/temperature

$\{L\} = \begin{Bmatrix} \frac{\partial}{\partial x} & \frac{\partial}{\partial y} & \frac{\partial}{\partial z} & 0 & 0 & 0 \\ 0 & 0 & 0 & \frac{\partial}{\partial x} & \frac{\partial}{\partial y} & \frac{\partial}{\partial z} \end{Bmatrix}^T$  is a differential operator.

In the above equation,

$[C^*]$  is the element humidity/heat capacity matrix

$[D^*]$  is the element humidity/heat diffusion matrix.

Based on the coupled humidity/temperature governing equations, Equations 1, 2, and 3:

$[C^*]$  and  $[D^*]$  have the following matrix forms:

$$[C^*] = \begin{bmatrix} C_h^* & 0 \\ 0 & \rho c \end{bmatrix}$$

and

$$[D^*] = \begin{bmatrix} \bar{D}_{hx} & 0 & 0 & \bar{D}_{Tx} & 0 & 0 \\ 0 & \bar{D}_{hy} & 0 & 0 & \bar{D}_{Ty} & 0 \\ 0 & 0 & \bar{D}_{hz} & 0 & 0 & \bar{D}_{Tz} \\ 0 & 0 & 0 & \lambda_x & 0 & 0 \\ 0 & 0 & 0 & 0 & \lambda_y & 0 \\ 0 & 0 & 0 & 0 & 0 & \lambda_z \end{bmatrix}$$

Using element shape functions defined in the matrix form as

$$\{N(x, y, z)\} = \begin{Bmatrix} N_1 & 0 & N_2 & 0 & \dots & N_r & 0 \\ 0 & N_1 & 0 & N_2 & \dots & 0 & N_r \end{Bmatrix}^T,$$

where  $r$  is the total number of nodes per element, and the element humidity/temperature vector can be discretized in terms of nodal humidity/temperature vector:

$$\begin{Bmatrix} h_i \\ T_i \end{Bmatrix} \quad (i=1,2,\dots,r)$$

as:

$$\begin{Bmatrix} h \\ T \end{Bmatrix} = \{N\}^T \begin{Bmatrix} h_i \\ T_i \end{Bmatrix} \quad \text{Eq 7}$$

Substituting Equation 7 into Equation 6, the finite element equation becomes:

$$[C_e^*] \begin{Bmatrix} \frac{\partial h_i}{\partial t} \\ \frac{\partial T_i}{\partial t} \end{Bmatrix} + [D_e^*] \begin{Bmatrix} h_i \\ T_i \end{Bmatrix} = \{Q_e\} \quad \text{Eq 8}$$

where:

$$[D_e^*] = \int_V [B]^T [D^*] [B] dV = \text{element humidity/heat diffusion matrix}$$

$$[C_e^*] = \int_V \{N\} [C^*] \{N\}^T dV = \text{element humidity/heat capacity matrix}$$

$$\{Q_e\} = \int_S \{N\} q^* dS = \text{element boundary humidity/heat flux}$$

$$[B] = \{L\} \{N\}^T$$

In the above finite element equation, the shape functions,  $\{N(x, y, z)\}$ , are polynomials in terms of the local coordinates of a finite element and are used to approximate the variations of the state variables, i.e., humidity and temperature, within each element. The values of the state variables at any location within the element can then be evaluated based on the nodal values of the state variables as expressed in Equation 7. The order of the polynomial used in the shape function will dictate the accuracy and the characteristics of the finite element numerical solution. In general, the higher the order of the shape function, the higher the accuracy of the solution. Nevertheless, it requires larger number of nodes per element and longer computation time to reach a solution.

Higher order nonlinear shape functions are generally more suitable for models with curved boundaries. Since there are no curved boundaries in the model employed, linear shape functions were used in the present analysis. Such a choice was based on the considerations for reducing computation time of the analysis in three-dimensional models as well as for avoiding the need to account for nonlinearities both in material properties and model shape functions.

To solve the transient problem, the finite element equation, Equation 8, was discretized by the generalized trapezoidal rule with respect to the time coordinate.

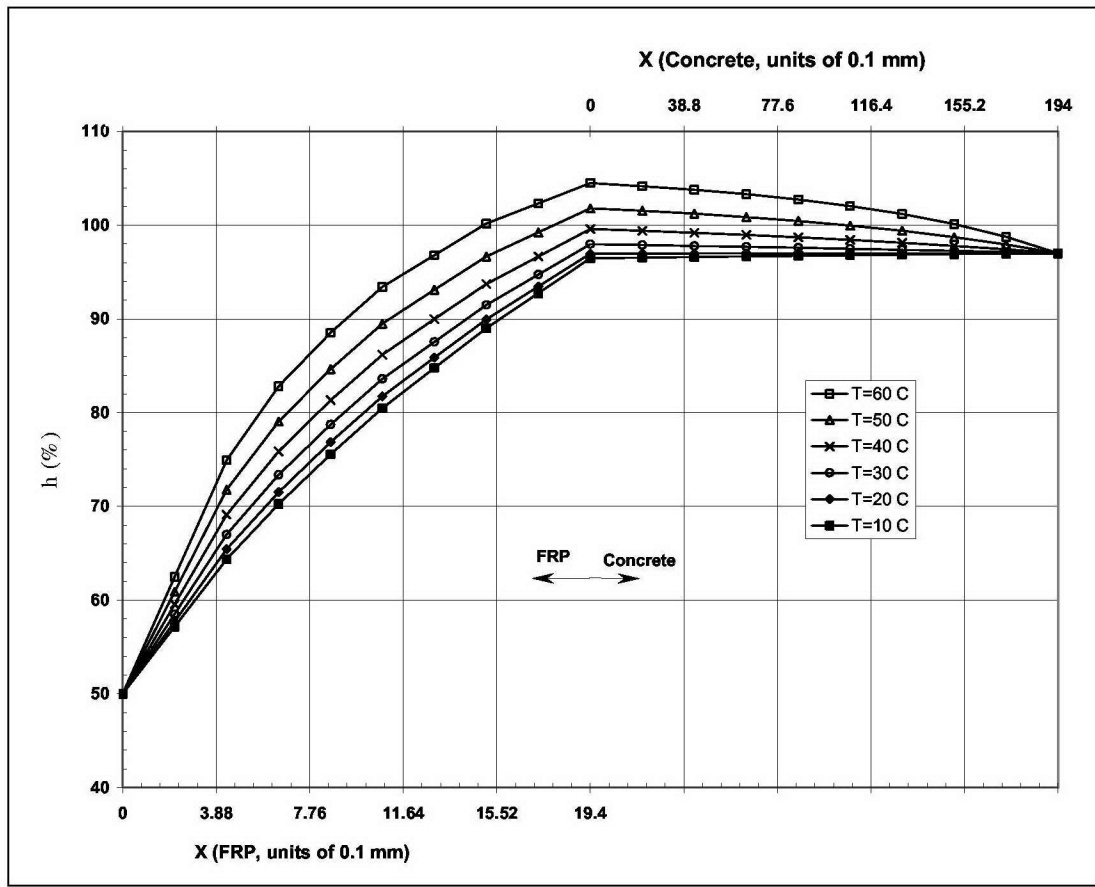
The resulting system of equations at the time instant was then solved by the iterative linearization method. Note that, at the first time instant, the diffusion matrix and the capacity matrix were computed based on the initial humidity and temperature conditions. Subsequently, their values were updated based on the solution of the humidity and temperature fields obtained. These values were then used for the next time step. The new system of equations was solved again and the procedure continued with increasing time instant until it reached the final desired time instant.

### Numerical Solutions for Moisture, Total FRP-CMU Coverage

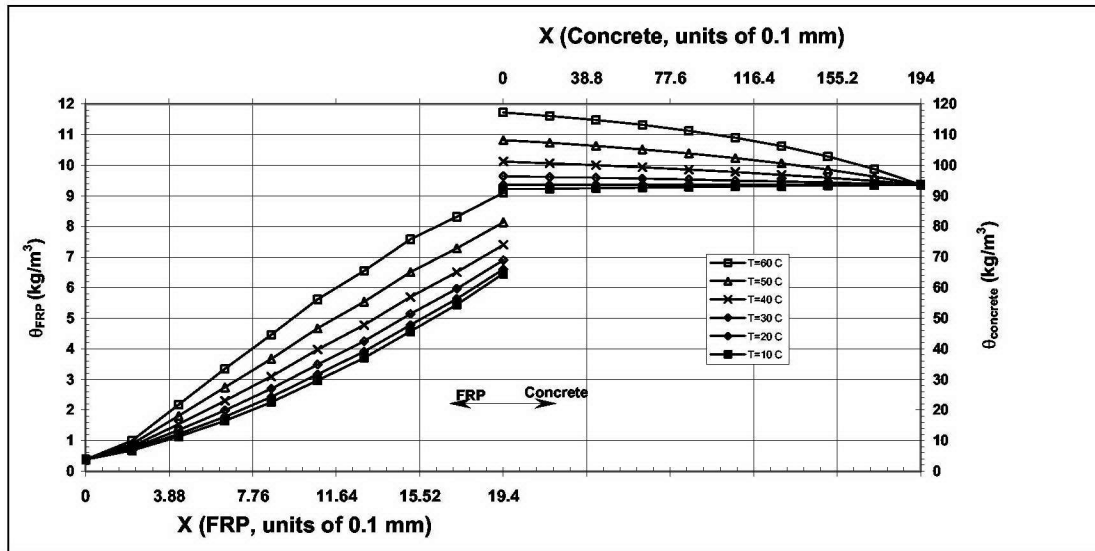
With the above finite element modeling tools at hand, a simple test case was run to provide a cross check for the proper functioning of the coupled computer codes, and a reality check from both physical and field experience. For this elementary case, the 2D problem shown in Figure 5 was further reduced to a 1D problem by having the FRP totally cover the CMU. The interior FRP surface was constrained to 50 percent RH and 20 °C, while the exterior surface RH was held at 97 percent RH with the temperature permitted to vary from 10 to 60 °C. As such, this simulation was representative of extreme hygrothermal external environments. Figures 6 and 7, respectively, show spatial distribution solutions (in a direction normal to FRP-CMU interface) of humidity,  $h$ , and total moisture,  $\theta$ . Each Figure is a composite of both FRP and CMU steady-state data for several temperatures extending from 10 to 60 °C. For this project, the FRP has a standard thickness of 1.94 mm and the CMU base has a standard thickness of 19.4 mm.

Figure 6 shows the humidity starting at 50 percent and rapidly rising monotonically towards the FRP-CMU interface, where there is a spread in RH,  $h$ , associated with temperature variations. The relative humidity fulfills the humidity continuity boundary condition (Equation 2) at the interface, and has a relatively smaller spread as it tends toward the 97 percent RH boundary condition on the outer surface of the CMU. This figure confirms the physical notion that most of the RH drop through the system will occur in the (oil-based) FRP. The CMU is relatively porous and, by comparison, more transparent to moisture migration. Thus the RH will be more or less constant across the CMU.

Further inspection reveals that the RH at the FRP-CMU interface increases monotonically with the outside temperature. Mathematically, this arises from the  $D\nabla T$  term in Equation 1, and again confirms the physical experience that a temperature gradient can act as a pseudo-moisture source.



**Figure 6.** 1D steady-state moisture transport problem, humidity profile, with FRP totally covering the CMU; the interior FRP surface is constrained to 50% RH and 20 °C, while the exterior surface RH is held at 97% RH with the temperature permitted to vary from 10 to 60 °C.



**Figure 7.** 1D steady-state moisture transport problem, total moisture density  $\theta$  profile, with FRP totally covering the CMU; the interior FRP surface is constrained to 50% RH and 20 °C, while the exterior surface RH is held at 97% RH with the temperature permitted to vary from 10 to 60 °C.

Closer inspection however, reveals a cautionary feature. For temperatures greater than 45 °C, it is seen that the RH is greater than 100 percent. Such supersaturation might suggest pooling or condensation of moisture in a laboratory experiment. However there is no physical mechanism for this condensation incorporated into the isothermal absorption curves for either FRP or CMU (Figure 1). This anomaly appears to originate from the fact that the isothermal absorption curves for FRP and CMU (Appendix A) are analytically continuous for all values of the relative humidity,  $h$ , even though the physical region of applicability is constrained to a RH of 98 percent or less (see the end of section 2.1). Thus the computer is able to converge a solution of questionable physical reality. However the trend is one that has a basis in reality. The thermal gradient is always from a warm surface toward a colder surface. As such, there exists a clear tendency for increased moisture at the cooler interface. An immediate consequence is to avoid total coverage of CMU in such extremes of humidity and temperature. This conclusion derives further support from the experience of exterior paint applications in cold climates (Korhonen and Bayer 1989), which cautions to provide ample ventilation of painted exterior masonry, to avoid paint delaminations, primarily from efflorescence.

Figure 7, by comparison, has many of the qualitative features found in Figure 6 with one significant difference, the discontinuity of the moisture density,  $\theta$ , across the FRP-CMU interface. This anticipated difference in moisture content makes (petroleum-based) paints effective in preserving wood from moisture uptake. Furthermore, a detailed analyses of the interfacial moisture gradients, the  $q + D\theta\nabla\theta + D_T\nabla T = 0$  of Equation 1, certifies that the moisture flux requirement of Equation 2 is also fulfilled. In summary, these collective results support the conclusion that the finite element computer program can provide useful results in keeping with physical intuition and field data, provided that the calculation returns values of the relative humidity within the hygroscopic range of a given isothermal sorption curve.

## Numerical Solutions for Moisture, Partial FRP-CMU Coverage

Drawing on the success of the previous 1D model, a calculation was performed for the 2D case shown in Figure 5. In this rendering, the FRP covers about 60 percent of the interior lateral surface (X-Z, plane). As in the 1D case, the interior FRP surface was constrained to 50 percent RH and 20 °C, while the exterior surface RH was held at 97 percent RH with the temperature permitted to vary from 10 to 60 °C. Spatial distribution solutions of humidity,  $h$ , and total moisture,  $\theta$ , were computed throughout the 2D structure (within the Y-X plane). However the middle of the CMU-FRP block contains a plane of symmetry with respect to

the “X” direction. Calculations performed in this plane (containing a “Y” axes) will have the highest values of humidity,  $h$ , and total moisture,  $\theta$ , relative to the corresponding uncovered portions of CMU. As such these centerline values provide a reasonable benchmark for comparison between the 1D and 2D cases.

Figures 8 and 9, respectively, show the steady-state humidity and total moisture as function of spatial distribution. Each Figure is a composite of both FRP and CMU data for several temperatures extending from 10 to 60 °C, and have the same FRP-base dimensions as before. Many of the global physical characteristics of these Figures are analogous to the 1D case. However, the relative humidity remains within physical limits for all temperatures. As in the 1D case, there is an analogous increase of humidity,  $h$ , and total moisture,  $\theta$ , with increasing external temperature arising from the  $D_T \nabla T$  term in Equation 1. Further inspection of Figures 8 and 9 reveals that both the humidity and total moisture are actually less at the FRP-CMU interface, than at the external boundary. This is the case for external temperatures of 50 °C or less, and again underscores the virtue of ventilating the CMU, even with only a minor fraction of the total surface area.

While Figures 8 and 9 provide quantitative information within the symmetry plane, Figure 10 shows a more dramatic portrayal of the overall *moisture flux* (within the X-Y plane). Figure 10 clearly depicts the evacuation routes available to moisture that might otherwise be trapped behind the CMU-FRP interface. Figure 11 shows the resulting combination if the X-Y humidity profile is superimposed on Figure 10. The moisture flux shown in Figure 11 appears to be normal to the surfaces of constant humidity, which is an expected result given that the flux,  $q$ , scales proportional to  $\nabla \theta$ .

Finally, additional information consolidated within Figures 8 and 9 relates to the thermal profiles. To converge a consistent solution for Equation set 1 to 3 involving the total moisture,  $\theta$ , an equivalent set of (steady-state) thermal information is also generated,  $T = T(r, \theta)$ . Restricting this solution set to the symmetry plane implied for Figures 8 and 9 results in the thermal profile of Figure 12. As in those cases, the Figure is a composite of both FRP and CMU steady-state data, with the interior FRP surface constrained to 50 percent RH and 20 °C (Centigrade), while the exterior surface RH was held at 97 percent RH with the temperature permitted to vary from 10 to 60 °C.

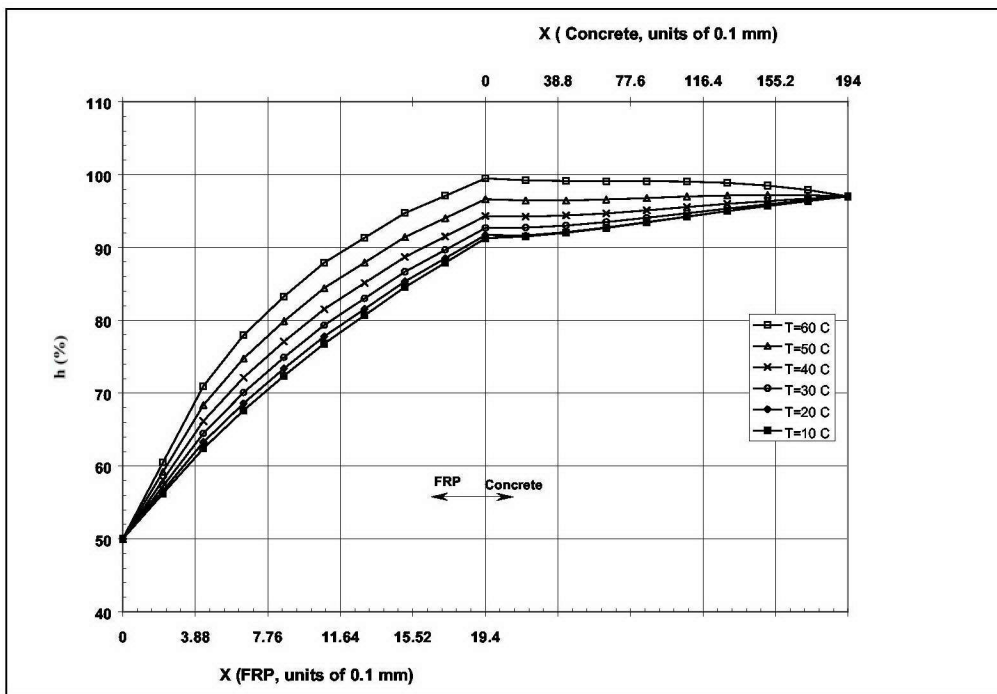


**Figure 8. 2D steady-state moisture transport problem, humidity profile, with FRP partially covering (~60%) the CMU; data taken from the (Y-Z) symmetry plane; the interior FRP surface is constrained to 50% RH and 20 °C; while exterior surface RH is held at 97% RH with the temperature permitted to vary from 10 to 60 °C.**

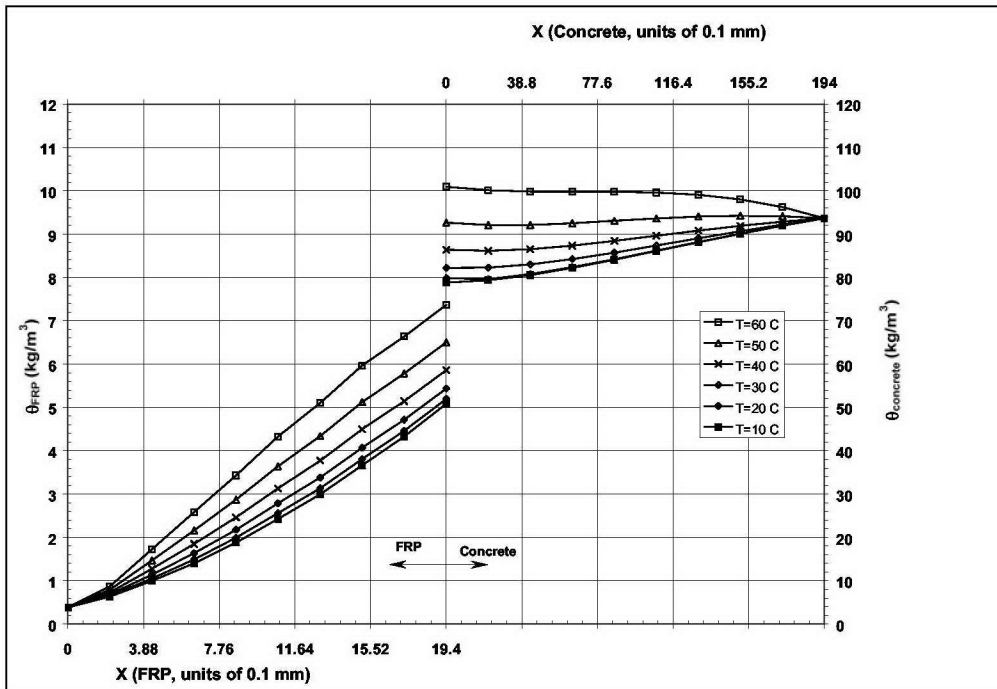


**Figure 9. 2D steady-state moisture transport problem, total moisture density  $\theta$  profile, with FRP partially (~60%) covering the CMU; data taken from the (Y-Z) symmetry plane; the interior FRP surface is constrained to 50% RH and 20 °C, while the exterior surface RH is held at 97% RH with the temperature permitted to vary from 10 to 60 °C.**

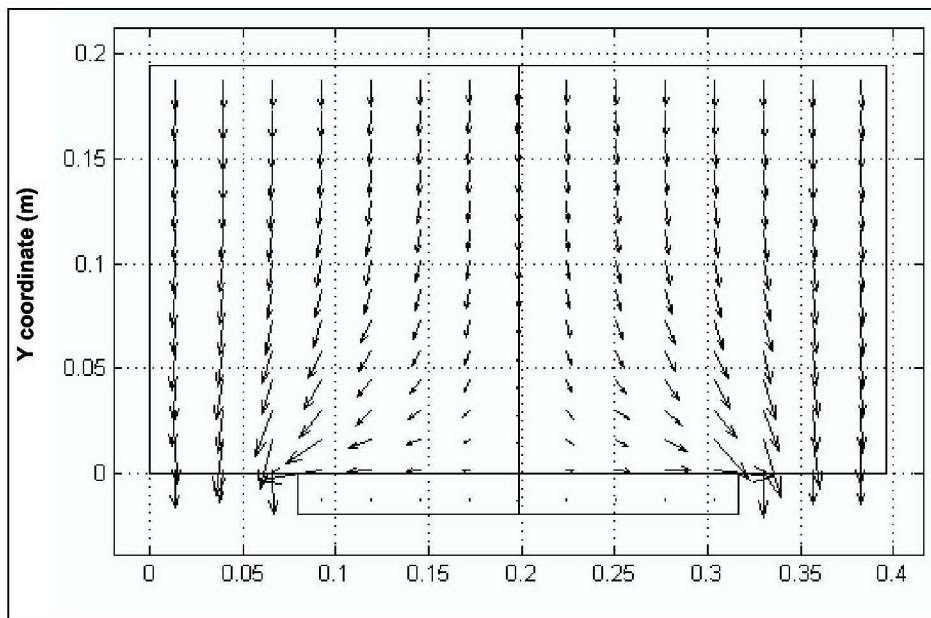


**Figure 10.** 2D steady-state moisture transport problem, depicting total moisture flux profile (within the X-Y plane), and FRP partially (~60%) covering the CMU; this chart delineates evacuation routes available to moisture that might otherwise be trapped behind the CMU-FRP interface; the interior FRP surface is constrained to 50% RH and 20 °C; the exterior surface RH is held at 97% RH with a temperature of order 20 °C.

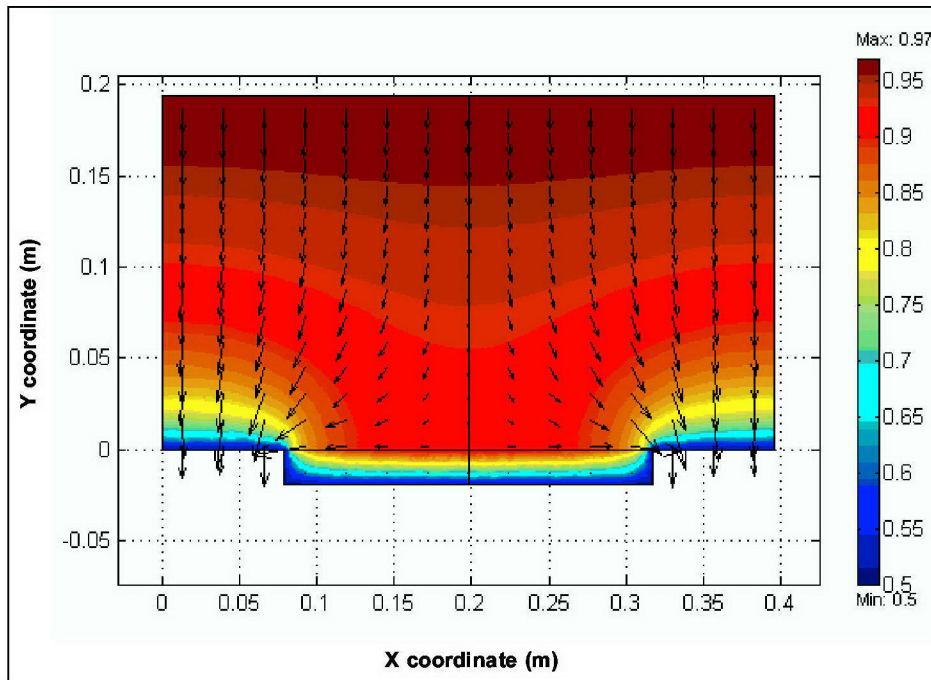


**Figure 11.** Figure 10, with the corresponding X-Y humidity profile superimposed. Note that the moisture flux appears to be normal to the surfaces of constant humidity, which is an expected result given that the flux,  $q$ , scales proportional to  $\nabla\theta$ , (see Equation 1).

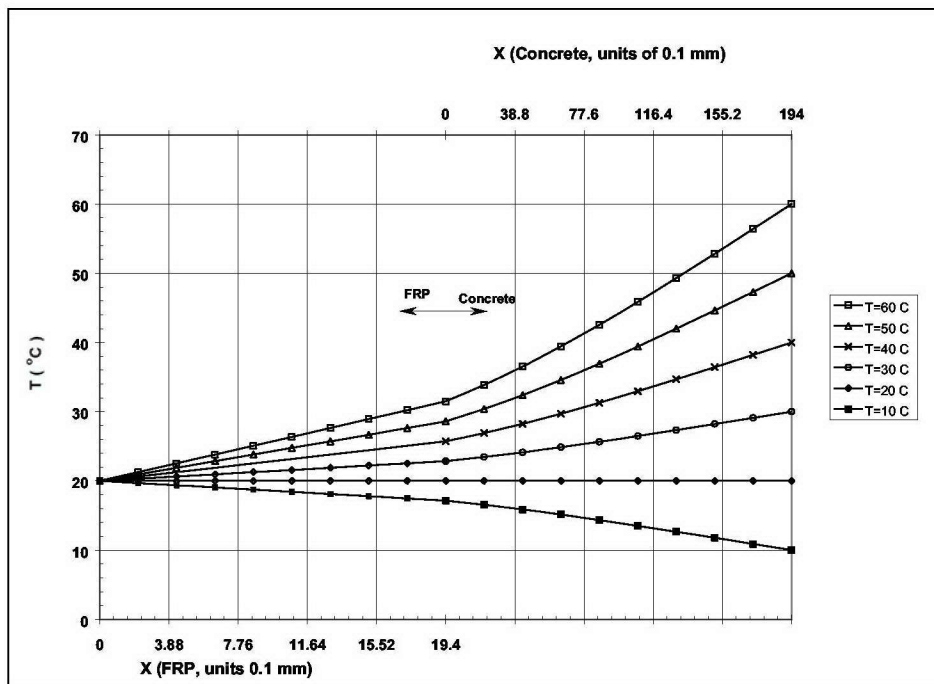


**Figure 12. FRP-CMU thermal profile, with FRP partially (~60%) covering the CMU; data taken from the (Y-Z) symmetry plane; the interior FRP surface constrained to 50% RH and 20 °C; exterior surface RH is held at 97% RH with the temperature permitted to vary from 10 to 60 °C.**

Figure 12 shows an almost linear profile of temperature as a function of distance through each of the FRP-CMU structures. This quasi-linear profile is the signature of an essentially constant thermal conductivity parameters,  $k_T$ , for the FRP-CMU system. A simple thermal flux calculation based on constant FRP-CMU material parameters (Appendix A), yields an interfacial temperature quite close to that resulting from the more exacting calculation shown in Figure 12. This observation verifies the prediction made at the end of section 2.3, regarding the role of temperature as a higher order parameter for the convergence of the total moisture solution. The resulting insensitivity tends to decouple the two solutions, and makes for efficient computer coding, at least for these particular building materials.

Closer inspection reveals a slight curvature in the thermal profiles of concrete and FRP. This reflects the small variation in,  $k_T$ , due to any explicit moisture sensitivity, as well the very slight contributions arising from the  $\nabla(hP_s(T))$  terms found in the “WUFI-ORNL/IPB” formulation (Kuenzel et al. undated [Oak Ridge]) of  $D_T \nabla T$  (see Appendix A, Equation A5). In fact, a detailed analyses of the thermal flux vector:

$$q_{Th} = \{k_T + h_v(\delta_p(T)/\mu)(\Delta H/RT^2)(hP_s(T))\}\nabla T$$

using the steady-state numerical data of Figures 12 and 9 reveals that the vector is conserved throughout the symmetry plane of the CMU-FRP. A consequence of this insensitivity to latent heat terms is that the interfacial temperature with and without corrections from the latent heat,  $h_v$ , differ by less than 0.05 percent for the stated variations in exterior temperatures.

## 4 Coupled Moisture, Temperature, and Structural Analysis

The completion of the hygrothermal calculation sets the stage for the mechanical analyses of moisture and temperature induced stresses in the FRP/concrete structure. This analysis was done by considering the moisture and temperature induced strains as applied forces in a way similar to the application of body forces as input parameters in standard structural analysis. The pre-defined structural analysis module provided in the FEMLAB was employed to carry out this coupled hygrothermal-mechanical analysis.

In the coupled hygrothermal-mechanical problem, the total apparent strain is the sum of the mechanical strain, the temperature induced strain due to thermal expansion, and the moisture induced strain due to moisture swelling effect. The mechanical strain thus can be calculated by the following equation:

$$\varepsilon_{mechanical} = \varepsilon_{total} - \varepsilon_{thermal} - \varepsilon_{moisture} = \varepsilon_{total} - \alpha\Delta T - \beta\Delta\theta, \quad \text{Eq 9}$$

where:

- $\alpha$  = the coefficient of thermal expansion (CTE)
- $\beta$  = the coefficient of moisture swelling.

The constitutive equation, which relates the stress and strain states in a solid medium, can then be expressed as:

$$\{\sigma\} = [D]\{\varepsilon_{mechanical}\} = [D]\{\varepsilon_{total} - \alpha\Delta T - \beta\Delta\theta\}, \quad \text{Eq 10}$$

where:

- $\{\sigma\} = \{\sigma_x \ \sigma_y \ \sigma_z \ \tau_{xy} \ \tau_{yz} \ \tau_{xz}\}^T$  is the stress vector
- $[D]$  is the stiffness matrix
- $\{\varepsilon_{total}\} = \{\varepsilon_x \ \varepsilon_y \ \varepsilon_z \ \gamma_{xy} \ \gamma_{yz} \ \gamma_{xz}\}^T$  is the total strain vector and can be related to displacements by the displacement-strain relation as:

$$\{\varepsilon_x \ \varepsilon_y \ \varepsilon_z \ \gamma_{xy} \ \gamma_{yz} \ \gamma_{xz}\}^T = \begin{Bmatrix} \frac{\partial}{\partial x} & 0 & 0 & \frac{\partial}{\partial y} & 0 & \frac{\partial}{\partial z} \\ 0 & \frac{\partial}{\partial y} & 0 & \frac{\partial}{\partial x} & \frac{\partial}{\partial z} & 0 \\ 0 & 0 & \frac{\partial}{\partial z} & 0 & \frac{\partial}{\partial y} & \frac{\partial}{\partial x} \end{Bmatrix}^T \begin{Bmatrix} u_x \\ u_y \\ u_z \end{Bmatrix} = \{L\} \begin{Bmatrix} u_x \\ u_y \\ u_z \end{Bmatrix} \quad \text{Eq 11}$$

Using the same finite element formulation approach as shown in Section 3.1, the resulting finite element equation for structural analysis incorporating moisture and temperature induced strains results in the following form:

$$[K]\{U\} = \{F_B\} + \{F_S\} + \{F_{\text{thermal}}\} + \{F_{\text{moisture}}\}, \quad \text{Eq 12}$$

where:

$$\{U\} = \{u_{x1} \ u_{y1} \ u_{z1} \ u_{x2} \ u_{y2} \ u_{z2} \ \dots \ u_{xr} \ u_{yr} \ u_{zr}\}^T = \text{nodal displacement vector}$$

$$[K] = \int_V [B]^T [D] [B] dV = \text{element stiffness matrix}$$

$$\{F_B\} = \int_V [N]^T \{F_b\} dV = \text{element body force vector}$$

$$\{F_S\} = \int_S [N]^T \{F_s\} dS = \text{element force due to surface traction}$$

$$\{F_{\text{thermal}}\} = \int_V [B]^T [D] \{\varepsilon_{\text{thermal}}\} dV = \text{element force vector due to thermal expansion}$$

$$\{F_{\text{moisture}}\} = \int_V [B]^T [D] \{\varepsilon_{\text{moisture}}\} dV = \text{element force vector due to moisture swelling.}$$

In the above expression,  $[B] = \{L\} \{N\}^T$ , in which  $\{L\}$  is defined in Equation 6, and:

$$\{N(x, y, z)\} = \begin{Bmatrix} N_1 & 0 & 0 & N_2 & 0 & 0 & \dots & \dots & N_r & 0 & 0 \\ 0 & N_1 & 0 & 0 & N_2 & 0 & \dots & \dots & 0 & N_r & 0 \\ 0 & 0 & N_1 & 0 & 0 & N_2 & \dots & \dots & 0 & 0 & N_r \end{Bmatrix}^T. \quad \text{Eq 13}$$

is the shape function matrix.

Since moisture migration in the structure was modeled in terms of humidity potential state variable instead of moisture content, the swelling coefficient,  $\beta$ , which is generally given as a function of moisture content, needs to be modified. The moisture induced strain in terms of moisture content can be computed as:

$$\varepsilon_{\text{moisture}} = \bar{\theta} \cdot \beta = \frac{\theta}{\rho} \beta, \quad \text{Eq 14}$$

where:

$$\bar{\theta} \left[ \frac{kg}{kg} \right] = \text{the specific moisture content and } \rho \text{ is the mass density of the material.}$$

The 3D model shown in Figure 4(a) was used for the coupled hygrothermal-mechanical analysis since the temperature and moisture induced stresses in the FRP/concrete structure need to be described in a three-dimensional state. A finite element mesh as shown in Figure 4(b) was generated using tetrahedral linear elements. The density of the mesh was chosen based on the considerations of numerical precision and the required computation time for a typical nonlinear analysis of the three-dimensional model. The material properties of the concrete (Baker 1964) and FRP (Tsai 1986) are given in Table 2, where the swelling coefficient,  $\beta$ , is approximated as a constant and is dimensionless, representing strain per unit-specific moisture content.

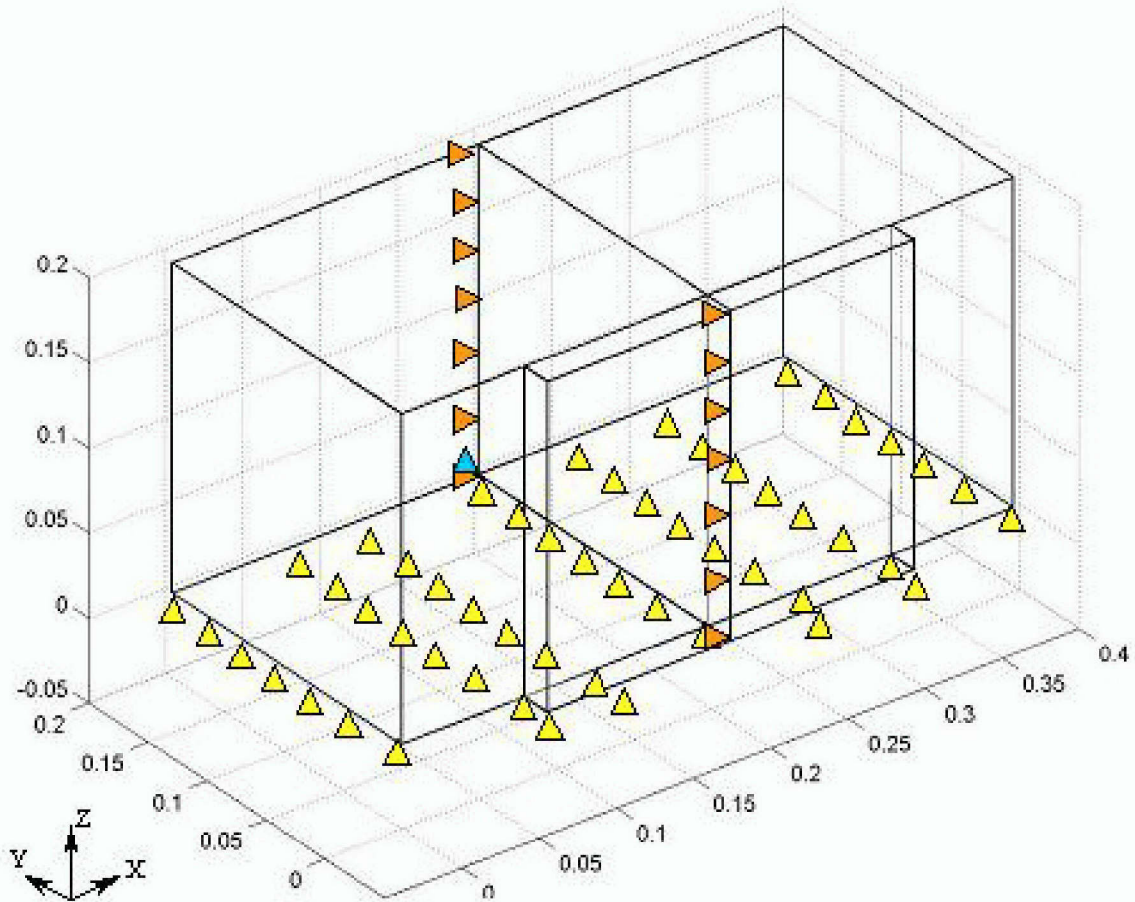
In the current study, a nominal dense concrete with  $\rho = 2140 \text{ kg/m}^3$  and a typical glass/epoxy FRP with density  $\rho = 1160 \text{ kg/m}^3$  were used. It is noted that the FRP lamina is a transversely isotropic material and the numeral subscripts were used to indicate its three principal axes. Along the direction of the fiber reinforcement, the moisture-induced swelling is negligible since the glass fibers are not permeable and have a much higher stiffness than the epoxy matrix.

Figure 13 shows the schematic of the model with prescribed displacement constraint boundary conditions. The nodal displacement  $u_z$  on the all nodes on the  $z = 0$  surface is constrained based on the consideration of symmetric boundary. The displacements in the  $x$  direction for the nodes on the central edges of the model with  $y = -0.0194$  and  $y = 0.194$  are also restrained.

**Table 2. Material Properties for concrete and FRP.**

Concrete			
E (Gpa)	v	$\beta$	$\alpha$
13.8	0.18	0.00767	$9.99 \times 10^{-6}$

FRP									
E <sub>1</sub> (Gpa)	E <sub>2</sub> , E <sub>3</sub> (Gpa)	G <sub>12</sub> , G <sub>13</sub> (Gpa)	G <sub>23</sub> (Gpa)	v <sub>12</sub> , v <sub>13</sub>	v <sub>23</sub>	$\beta_1$	$\beta_2, \beta_3$	$\alpha_1$	$\alpha_2, \alpha_3$
38.6	8.27	4.14	3.45	0.26	0.2	0	$0.6 \times 10^{-6}$	$8.6 \times 10^{-6}$	$22.1 \times 10^{-6}$



**Figure 13. Schematic of displacement boundary conditions.**

Finally, to prevent rigid body motion in the  $y$  direction,  $y$ -displacement of the node at the coordinates of  $x = 0.198$ ,  $y = 0.194$  and  $z = 0$  is also restrained.

The indoor and outdoor boundary conditions were prescribed as  $T_{in} = 20^\circ\text{C}$  and  $T_{out} = 60^\circ\text{C}$  for temperature, and  $h_{in} = 50\%$  and  $h_{out} = 97\%$  for relative humidity. Figures 14 and 15, respectively, show the resulting steady-state temperature and relative humidity contours. It can be seen that the humidity and temperature distributions are two-dimensional. Also, the thermal conductivity of the FRP is on average only one fifth that of the concrete, a higher temperature gradient is therefore shown in the FRP laminate. Because the FRP laminate only covers the central portion of the concrete slab, the resulting temperature profile is non-uniform and thus the heat flux flows are not parallel. It can be seen that the maximum temperature gradient in the FRP region exists at the centerline.

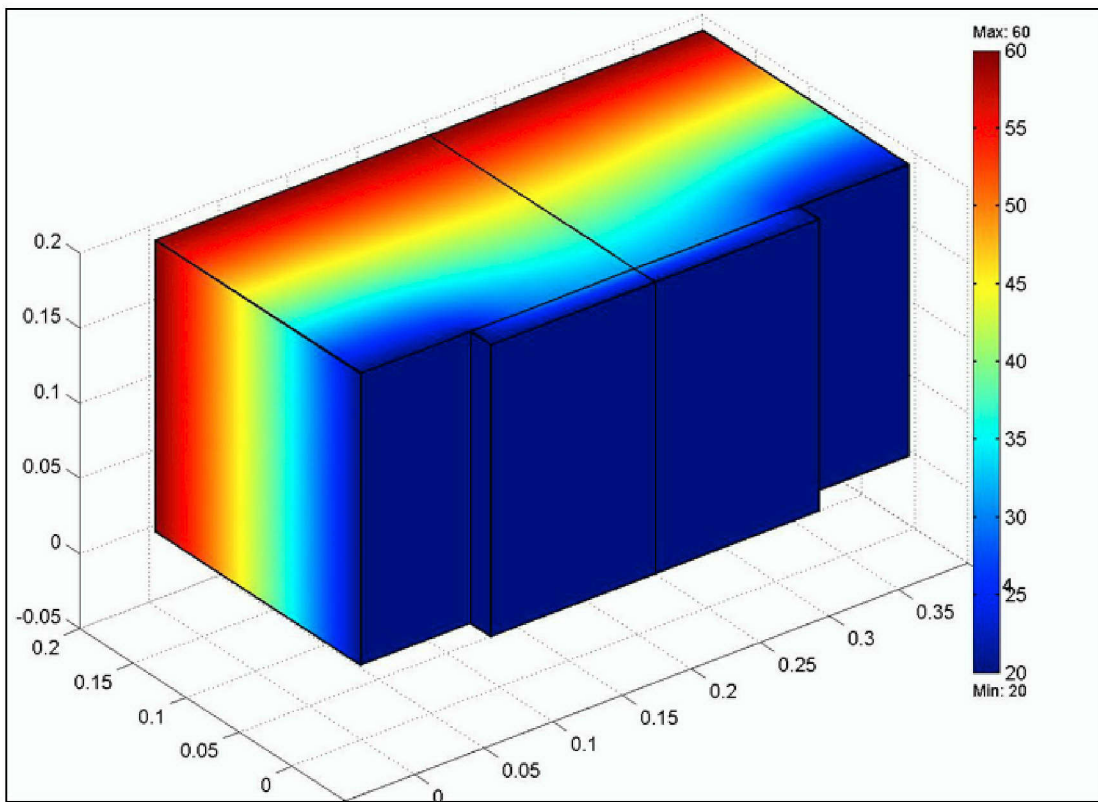


Figure 14. Temperature contour of the concrete slab partially covered with an FRP laminate (°C).

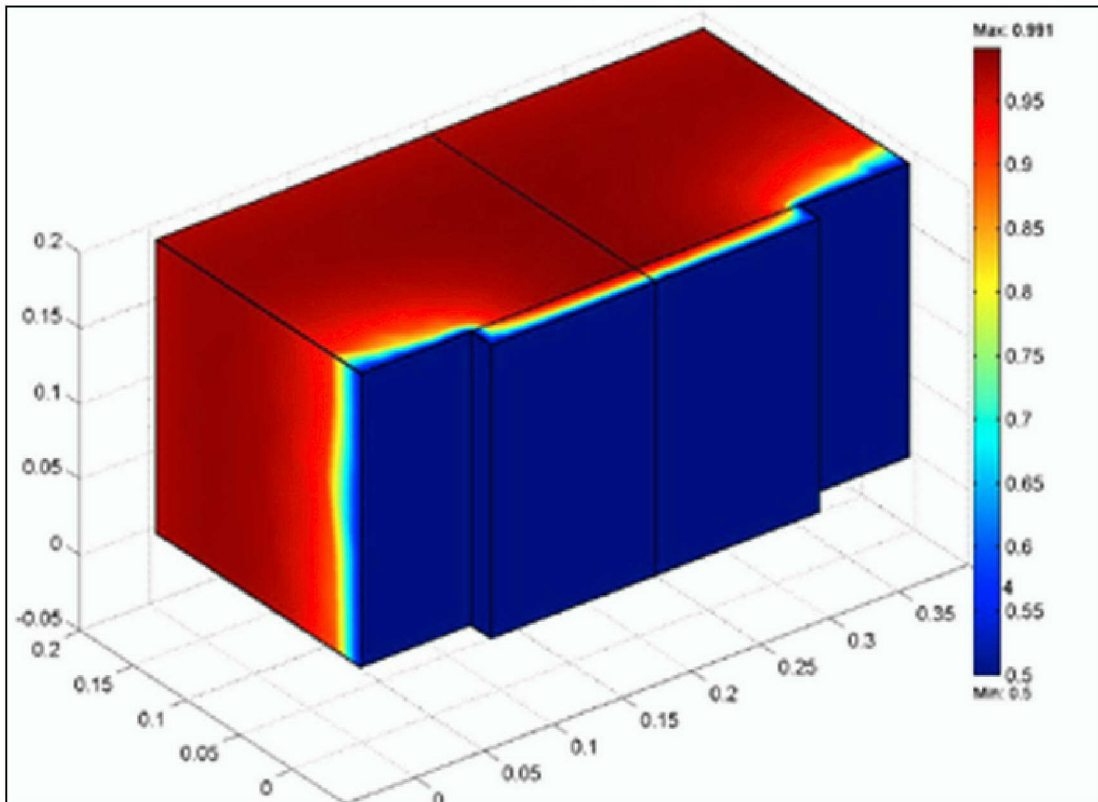


Figure 15. Relative humidity contour of the concrete slab partially covered with an FRP laminate.

Both the humidity and thermal humidity diffusion coefficients for concrete are much higher than those of the FRP. In average, they are 2300 and 560 times greater, respectively. A much higher humidity gradient therefore is shown in the FRP region. This pattern is similar to that of the temperature distribution profile. Again, the resulting humidity distribution profile is non-uniform and the humidity flux flows are not parallel. The FRP laminate behaves as a moisture barrier in the regards of moisture diffusion.

Figures 16 and 17, respectively, show the resulting contours for the interfacial nodal shear stress  $\tau_{xy}$  for the concrete and FRP regions. This stress quantity represents the degree of shearing mechanism induced on the surface normal to the y-axis, i.e., x-z plane, with the direction along the x-axis. It is the stress component responsible for interfacial shear debonding in the transverse direction. It can be seen that the extreme value of this stress quantity occurs at the discontinuous interface between the concrete and FRP, and that the stress gradually returns to the equilibrium value within a distance that is five to six times the characteristic FRP thickness. This relaxation phenomenon is a general feature of dissimilar materials in intimate contact, subject to different quantities of strain and is known as "Saint-Venant's" principle.

Figure 18 shows the contour for the displacement component  $u_x$  on the deformed geometry of the model on the x-y plane. It is evident that the concrete slab tends to expand more than the FRP due to the combined effect of thermal expansion and moisture swelling. As a result, this mismatch in the expansion in the concrete and FRP causes the interlaminar shear stress in the x-direction. Since  $\tau_{xy}$  shear stress acts in two opposite directions on the two edges at the FRP-concrete interface, the stresses along these edges have opposite signs. Some shearing stresses are also observed on the side surfaces of the concrete, i.e., at the  $x=0$  and  $x=0.396$  planes, and the  $z=0.194$  plane. These stresses are apparently caused by the warping deformation about the z- and y- axes, respectively.

Figures 19 and 20, respectively, show the resulting contours for the interfacial element shear stress  $\tau_{yz}$  for the concrete and FRP regions. Based on the available material property data, the FRP has no moisture swelling effect in the z direction (the fibers severely constrain swelling in this direction), while the concrete slab expands due to moisture in this direction. Mechanical interaction mechanism similar to that discussed above also occurs in the z-direction, resulting in maximum interlaminar shearing stress  $\tau_{yz}$  at the interface of concrete and FRP.

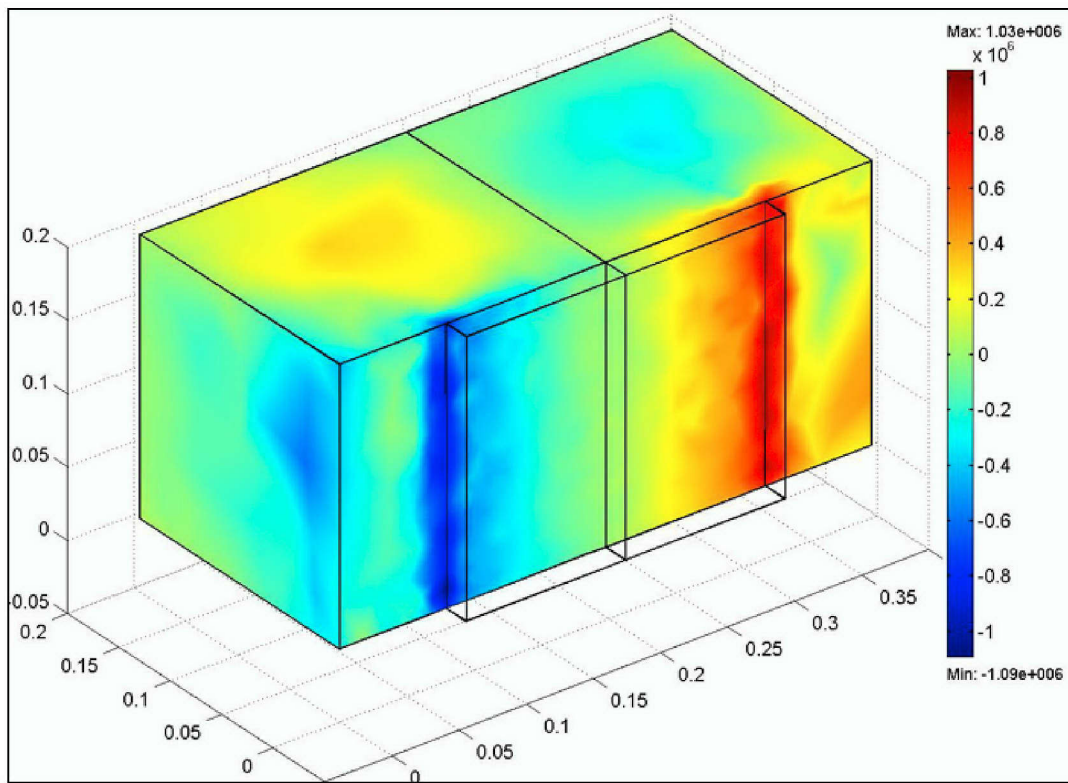


Figure 16.  $\tau_{xy}$  shear stress contour in the concrete slab (Pa).

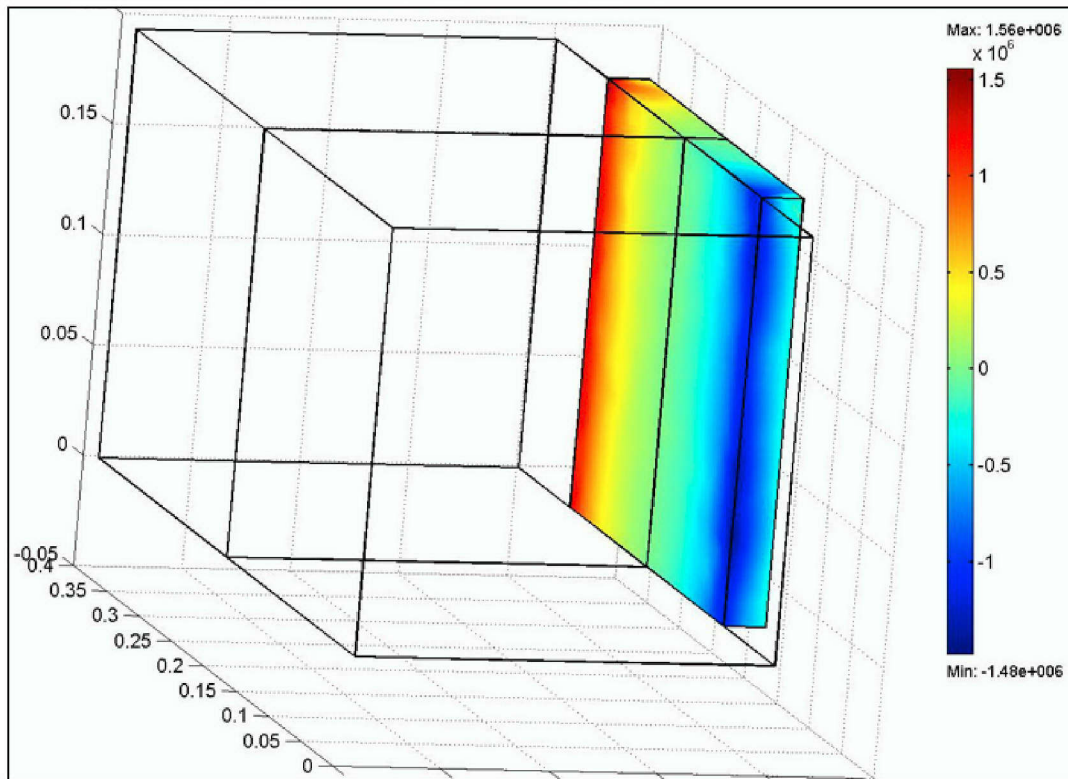
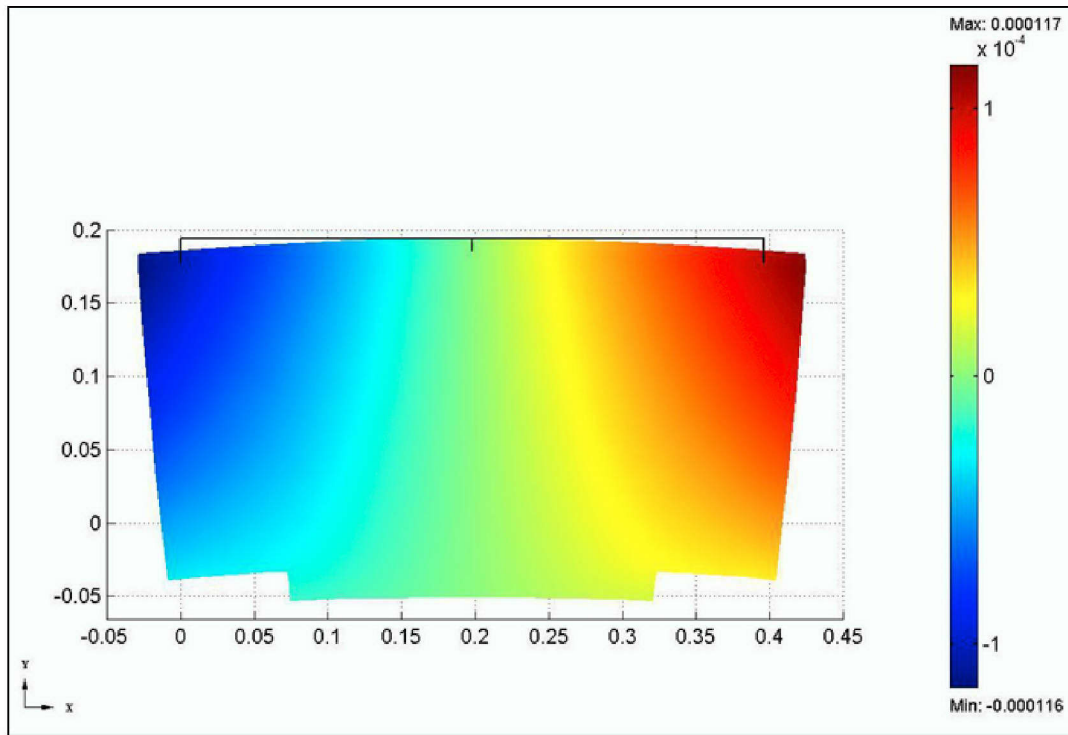
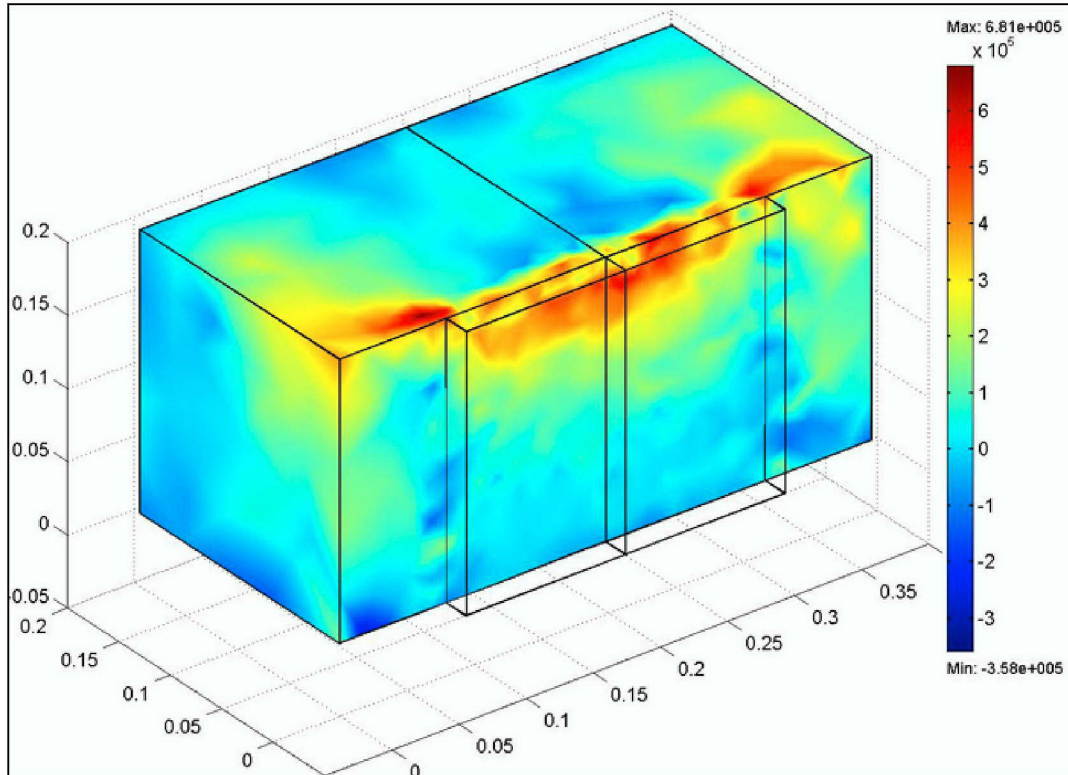


Figure 17.  $\tau_{xy}$  shear stress contour in the FRP laminate (Pa).



**Figure 18.** Displacement  $u_x$  contour depicted on the deformed geometry of the model on the x-y plane (m).



**Figure 19.**  $\tau_{yz}$  shear stress contour in the concrete slab (Pa).

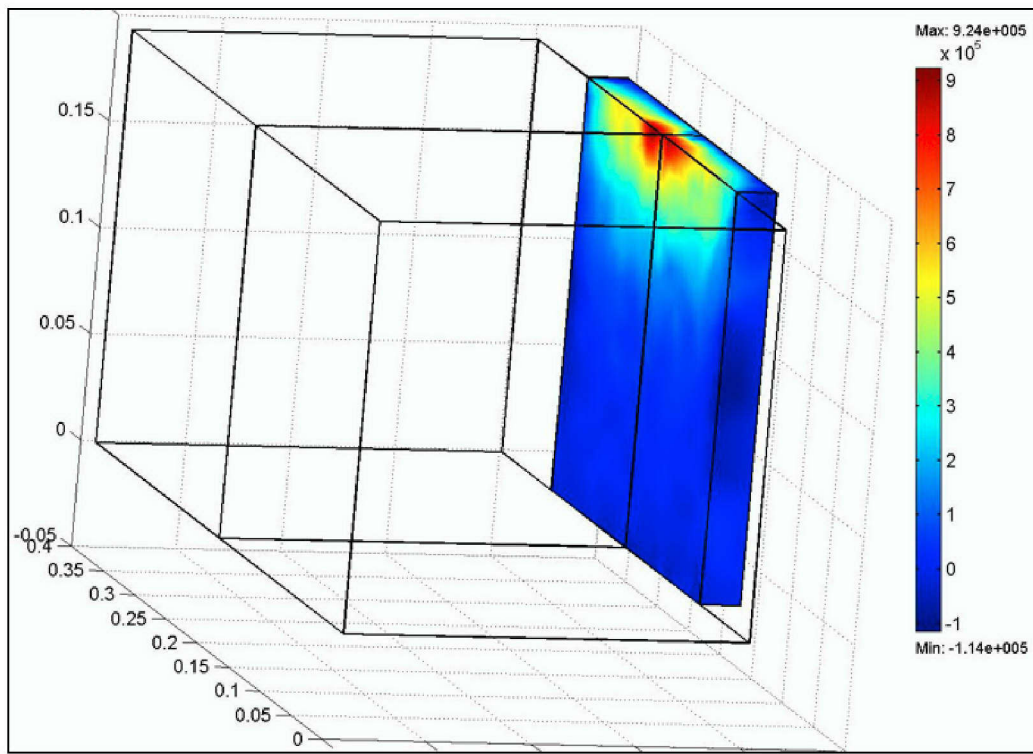


**Figure 20.**  $\tau_{yz}$  shear stress contour in the FRP laminate (Pa).

In addition, the nodal displacement  $u_z$  was constrained on the bottom surface to simulate the symmetric boundary condition. No interlaminar shear stress  $\tau_{yz}$  is induced in the area near the bottom surface. The  $\tau_{yz}$  stress contour, therefore, is symmetric with a mirror image about the bottom surface.

The coupled thermal and moisture shear stresses  $\tau_{xy}$  and  $\tau_{yz}$ , always coexist with other mechanical stresses within the FRP-CMU system. Under certain circumstances, these stresses can approach the tensile strength of the concrete substrate. A common engineering rule of thumb dictates that concrete will fail in tension at about 10 to 15 percent of its compressive strength (Ferguson 1979). A typical concrete might have a compressive strength on the order of 4000 PSI ( $2.71 \times 10^7$  Pa), and thus fail in tension at about  $3.0 \times 10^6$  Pa. Examination of  $\tau_{xy}$  in Figure 16, indicates that the maximum concrete stress to be about  $1.0 \times 10^6$  Pa, for the stated extreme conditions. Laboratory and field data suggest that, when FRP appliques debond from a CMU substrate, they do so by (tensile) failure of the substrate. Thus the finite element method provides a valuable metric for the qualification of what particular hygrothermal circumstances may lead to debonding of the FRP substrate.

Finally, since all the results presented here are for steady state conditions, it is helpful to get some measure of relevant time constants associated with transient

changes in moisture and temperature. Dimensional analyses, applied to equations 1 and 3 readily give the following characteristic time constants for changes in the moisture content of the system:

$$T_\theta = d^2/D_\theta$$

Here  $d$  and  $D_\theta$  are the material thickness and moisture diffusion constant (Appendix A), respectively. Using characteristic values of total moisture,  $\theta$ , from Figure 9 for CMU-FRP and  $d = 2$  cm for CMU and 0.2 cm for FRP, one finds that  $T_\theta \approx 100$  hrs for CMU and  $T_\theta \approx 730$  hrs for FRP. A similar analyses from Equation 3 yields:

$$T_{thm} = \rho c d^2/k_T$$

Again using characteristic values of total moisture,  $\theta$ , from Figure 9 for CMU-FRP and  $d = 2$  cm for CMU and 0.2 cm for FRP, one finds that  $T_{thm} \approx 5.2$  min for CMU and  $T_{thm} \approx 17.6$  sec for FRP.

With these characteristic time constants for the moisture and thermal change of a system, it is possible to estimate a characteristic strain rate of change,  $d\varepsilon/dt$ , for a given unit step change in the moisture,  $\theta$ , and temperature  $T$ . Using typical values of  $\beta$  and  $\alpha$  from Table 2, one finds a moisture induced strain rate:

$$d\varepsilon/dt \approx 3.5 \times 10^{-8} \text{ (strain) / hour for concrete, and}$$

$$d\varepsilon/dt \approx 5.13 \times 10^{-13} \text{ (strain) / hour for FRP.}$$

Similarly, a corresponding thermal induced strain rate is:

$$d\varepsilon/dt \approx 1.2 \times 10^{-4} \text{ (strain) / hour for concrete, and}$$

$$d\varepsilon/dt \approx 4.4 \times 10^{-3} \text{ (strain) / hour for FRP.}$$

FRP is then seen to contribute the dominant transient thermal strain to the system, and a secondary transient contribution derives from the concrete (CMU). These strains coexist as the system evolves in time depending on prevailing boundary conditions. And a corollary derived from these dissimilar rates of strain change is directly applicable to experimental design. Any simulation attempting to emulate natural changes in the environment, must take into account the global changes in the CMU-FRP system that will have vastly differing time constants, depending on the actual physical parameters and size of a given system. This further underscores the need for an explicit coupled hygrothermal calculation utilizing the finite element methods, to resolve the combined strain contribution in the CMU-FRP system.

## 5 Conclusions

This work has developed a generic finite element formulation for coupled hygrothermal-mechanical analysis for layered structures. The theoretical model follows that of Philip and De Vries, for mass and heat transport in a porous media and is used as the basis for the present work. To model moisture and temperature transport in structures with differing physical properties, an appropriate continuous moisture representation is required. This is because the total moisture content state variable, given in the mass and heat governing equations is discontinuous at the interfacial surfaces. In this work, the relative humidity of the surrounding air, which is related by the sorption isotherm relations to total moisture, was chosen as the continuous variable and resulted in a set of coupled governing equations.

Based on these modified governing equations, a finite element formulation was developed and implemented using the FEMLAB finite element analysis package. Solutions to this set of coupled equations resulted in 2D level curves, representing the thermal and moisture distributions within the FRP-CMU system plus its defining boundary conditions. The resulting moisture and temperature induced stresses in the FRP-CMU structure were then analyzed using the humidity and temperature distributions as parameters to define the body force inputs in a structural analysis program. To accomplish this, the predefined structural analysis mode, provided in the FEMLAB software package, was modified and employed to carry out the structural analysis. The resulting interfacial shear stresses caused by the mismatch of the thermal expansion and moisture swelling between the concrete and FRP were obtained.

Continuing, some conclusions derived from the documented research literature and simulations conducted in this research effort are:

1. When FRP is applied to interior CMU surfaces, it is known from laboratory studies that for the sake of both economy and mechanical response, unidirectional FRP reinforcement in the form of fabric strips is preferable to fabric that covers the whole surface of masonry walls (Triantafillou 1998; Rivera, Karbhari 2002), particularly if the FRP applique is deployed in extremes of humidity and temperature.

Further, this type of applique is to be applied to clean, unpainted CMU so as to

enhance both surface adhesion and free flowing ventilation of the CMU, thus avoiding moisture pooling. This consideration derives further support from the experience of exterior paint applications in cold climes (Korhonen Bayer 1989), which cautions to provide ample ventilation of painted exterior masonry, to avoid paint delaminations, primarily from efflorescence.

Finally, the requirement of a freely ventilated surface can be particularly crucial for a porous system containing both invading and receding fluids [Aker 1996; Descamps, 1997]. Water imbibition into porous building materials is a two-phase flow process in which the imbibing water displaces the air that is initially present in the pore space. Accurate non-destructive measurements of transient moisture profiles during imbibition into calcium silicate brick indicate that the air outflow boundary condition has a predominant influence on the water imbibition process. As a consequence, significant differences have been observed in the water sorption and transport coefficients derived from water imbibition experiments with free and bounded air outflow boundary conditions.

2. For extreme conditions of moisture and temperature differentials, such as encountered in the simulations of this research effort, debonding of the FRP from the CMU substrate is possible. This comes about because the coupled thermal and moisture shear stresses  $\tau_{xy}$ , always coexist with other mechanical stresses within the FRP-CMU system. Under certain circumstances, these stresses can approach the tensile strength of the concrete substrate. Laboratory and field data suggest that when FRP appliques debond from a CMU substrate, that they do so by (tensile) failure of the substrate. Furthermore, any experimental or computer simulation attempting to emulate natural environmental changes must take into account the global changes in a CMU-FRP system that will have vastly differing time constants, depending on the actual physical parameters and size of a given system. This further underscores the need and contributions from an explicit coupled hygrothermal calculation, using finite element methods. Doing so can resolve the combined strain rates in a given CMU-FRP system that may contribute to FRP-substrate debonding.
3. The boundary conditions used in the mechanical stress simulations of this report are that: The inside surface, is partially covered (60 percent) with FRP and is constrained to 50 percent RH and 20 °C, while the exterior surface is held at 97% RH and the temperature at 60 °C. As such, the results derived from these stress simulations must be viewed as somewhat extreme, so that *actual field conditions* of moisture and temperature gradients will in all reality be less severe.

Given this, the actual simulated shear stresses (item 2. above) were less than the tensile strength of the underlying CMU by at least a factor of three. This conclusion is supportive of, and consistent with a decade of field data that continues to

justify and champion the use of FRP upgrades for URM, when done in a consistent and conscientious manner by trained professionals.

4. The research literature cautions that the true kinetics of moisture absorption (FRP/CMU) under freeze-thaw exposure in *aqueous solutions*, is not well understood because of the presence of microcrack and fiber-matrix debond related degradation and possible mass dislocation (Rivera and Karbhari 2002). This work considered only the hygroscopic transport of water through a CMU-FRP system for temperatures greater than 0 °C but less than ~95 °C. Given this limitation, a natural recommendation, deriving from items 2. and 3. above, is to extend the present modeling and simulation effort to temperatures below the freezing point of water. In this temperature range, the physical properties and limitations of epoxies and FRP are anticipated to dominate those of the CMU substrate.
5. Appendix A to this report lists the required physical parameters that appear in the defining hygrothermal Equation set 1 to 3. These parameters were extracted, compiled and documented from the available (unclassified) research literature. Every attempt has been made to validate and cross reference these parameters, to ensure their correctness and validity. This validation procedure involved the painstaking checking of all data for consistency of units [MKS], compatible and relevant usage. In some cases, differing representations of the same physical constant and its hygrothermal representations existed. For these cases, every attempt was made to search the available research literature and seek out the most consistent and well founded representation. As such, the Appendix of this report represents one of the major contributions associated with this work unit, and can be an invaluable resource to the knowledgeable practitioner in this field.

## References

Agrawal, B.D., and L.J. Broutman, *Analysis and Performance of Fiber Composites* (John Wiley & Sons, Inc., New York, NY, 1990).

Aker, E., *A Simulation Model for Two-Phase Flow in Porous Media*, Ph.D. dissertation (Dept. of Physics, University of Oslo, Norway, c. 1996-97), available through URL: [www.fys.uio.no/~eaker/thesis/thesis.html](http://www.fys.uio.no/~eaker/thesis/thesis.html)

Al-Chaar, G.K., and H.A. Hassan, "Dynamic Response and Seismic Testing of CMU Walls Rehabilitated with Composite Material Applied to Only One Side," *Structures & Buildings Journal, Special Issue: Dynamic Behavior and Earthquake Design*, vol 152, No. 2 (2002), pp 135-146.

Anand, S.C., A. Gandhi., "A Finite Element Model To Compute Stresses in Composite Masonry Walls Due to Temperature, Moisture, and Creep," *Proceedings of the Third Canadian Masonry Symposium, 6-8 Jun 1983, Edmonton, Alberta* (1983), pp 34.1-34.20.

Baker, M C., "Thermal and Moisture Deformations in Building Materials," *Canadian Building Digest*, CBD-56 (Institute for Research in Construction, National Research Council Canada, 1964).

Celia, M.A., P.C. Reeves, and L.A. Ferrand, "Recent Advances in Pore Scale Models for Multiphase Flow in Porous Media," *Rev. Geophys.*, vol 33, suppl. (1995), available through URL: <http://www.agu.org/revgeophys/celia01/celia01.html>

Chern, B., T.J. Moon, and J.R. Howell, *Experimental Heat Transfer*, vol 6 (1993), p 157.

Chin, J.W., T. Nguyen, and K. Aouadi, *Journal of Applied Polymer Science*, vol 71, No. 3 (1999), p 483.

Claesson, J., *A Few Remarks on Moisture Flow Potentials*, Report TVBH-7163 (Division of Building Physics, Lund Institute of Technology, Lund University, Sweden, 1993).

Comyn, J., *Polymer Permeability* (Elsevier Applied Science Publishers, London and New York, 1985), ch 2-3, pp 11-117.

Descamps, F., *Continuum and Discrete Modeling of Isothermal Water and Air Transfer in Porous Media*, Ph.D. Thesis (Catholic University of Leuven, Belgium, 1997).

Ferguson, P.H., *Reinforced Concrete Fundamentals*, 4<sup>th</sup> ed. (Wiley & Sons, New York, 1979).

Ferry, J.D., *Viscoelastic Properties of Polymers*, 3d ed. (John Wiley and Sons Inc., New York, 1980).

Halpin, J.C., *Primer on Composite Materials: Analysis* (Technomic, Stamford, CT, 1984).

Hashin, Z. "Assessment of the Self-Consistent Scheme Approximation: Conductivity of a Particulate Composite," *Journal of Composite Materials*, vol 2, No. 3 (1968), pp 284-300.

Kim, J.K., and C.S. Lee., "Prediction of Differential Drying Shrinkage in Concrete," *Cement and Concrete Research*, vol 28, No. 7 (1998), pp 985-994.

Korhonen, C.J., Bayer, J.J., Jr., *Performance of Wall Coatings for Concrete and Masonry Buildings in Alaska*, Special Report 89-36 (Cold Regions Research and Engineering Laboratory [CRREL], November 1989).

Kuenzel, H., Karagiozis, A., Holm, A., WUFI ORNL/IBP Model 90 (Oak Ridge National Laboratory, and Fraunhofer Institute for Building Physics, 2000), available through URL: <http://www.ornl.gov/ORNL/BTC/moisture/>  
(Note: WUFI is a trademark of the Fraunhofer Institute for Building Physics).

Kumaran, M.K. Report IEA Annex XXIV, NRCC-38795, *Task 3: Material Properties International Energy Agency Annex 24 on Heat, Air and Moisture Control in Building Envelope Parts* (Publications Sales, M-20, Institute for Research in Construction, National Research Council Canada, Ottawa, Canada, K1AOR6, 1996), 135 pp.

Kunzel, H.M., *Simultaneous Heat and Moisture Transport in Building Components: One and Two-Dimensional Calculation Using Simple Parameters* (IRB Verlag, Stuttgart, 1995).

Lefebvre, D.R., D.A. Dillard, and T.C. Ward, "A Model for the Diffusion of Moisture in Adhesive Joints (Parts 1 & 2)," *J. Adhesion*, vol 27 (1989), pp 1-40.

Luikov, A.V., *International Journal of Heat and Mass Transfer*, vol 18, No. 1 (1975), pp 1-14.

Marshall, O.S., S.C. Sweeney, and J.C. Trovillion, "Seismic Rehabilitation of Unreinforced Masonry Walls," *Proceedings of the 4th International Conference on Fiber Reinforced Plastics for Reinforced Concrete Structures (FRPRCS-4) Oct/Nov 1999, Baltimore, MD*, (1999), pp 287-295.

Mårten Janz, "Methods of Measuring the Moisture Diffusivity at High Moisture Levels," Licentiate Thesis, report TVBM-3076 (Lund Institute of Technology, Division of Building Materials, Lund University, Sweden, 1997), available through URL: <http://www.ldc.lu.se/lthbml>

Pel, L., Center for Material Research with Magnetic Resonance (Eindhoven University of Technology, Department of Physics, PO Box 513, 5600 MB Eindhoven, The Netherlands), available through URL: [www.phys.tue.nl/nfcmr/cmmain.html](http://www.phys.tue.nl/nfcmr/cmmain.html)

Pel, L., *Moisture Transport in Porous Building Materials*, Dissertation (Eindhoven Univ. of Techn., Eindhoven, The Netherlands, 1995).

Philip, J.R., and D.A. De Vries, *Trans. Am. Geophys. Un.*, vol 38, No. 2, p 222 (1957).

Rivera, J., V.M. Karbhari, "Cold-Temperature and Simultaneous Aqueous Environment Related Degradation of Carbon/Vinylester Composites," *Composites*, pt B, vol 33 (2002), pp 17-24.

Saadatmanesh, H., "Extending Service Life of Concrete and Masonry Structures with Fiber Composites," *Construction and Building Materials*, vol 11, No. 5-6 (1997), pp 327-335.

Sakata, K., "A Study of Moisture Diffusion in Drying and Shrinkage of Concrete," *Cement and Concrete Research*, vol 3 (1983), pp 216-224.

Springer, G.S., *Environmental Effects on Composite Materials* (Technomic, Westport, CT, 1981).

T.C. Triantafillou, "Composites: A New Possibility for the Shear Strengthening of Concrete, Masonry and Wood," *Composites Science and Technology*, vol 58 (1998), pp 1285-1296.

Tsai, S.W. and Hahn, H.T., *Introduction to Composite Materials*, TECHNOMIC Publishing Co., Inc., 256 Post Road West, CT 06880, 1980.

Valen, Marit S., *Moisture Transfer in Organic Coatings on Porous Materials: The Influence of Varying Environmental Conditions*, Ph.D. Thesis NTNU N-7034 (Dept. of Building and Construction Engineering, Norwegian University of Science and Technology, Trondheim, Norway, August 1998), available through URL: <http://www.bygg.ntnu.no/batek/personal/valen/dravh.htm>

Van Geem, M.G., Fiorato, A.E., DOE/CE/30739-T1/DE83 011760, *Thermal Properties of Masonry Materials for Passive-Solar Design: A State-of-the-Art Review* (U.S. Department of Energy [DOE], Washington DC, April 1983).

van Zijl, G.P.A.G., *Series 11 Engineering Mechanisms: A Numerical Formulation for Moisture Migration in Masonry* (Delft University Press, P.O. Box 98, 2600 MG Delft, Netherlands 1999).

Verghese, K.N.E., M.D. Hayes, K. Garcia, C. Carrier, J. Wood, J.R. Riffle, and J.J. Lesko, *Journal of Composite Materials*, vol 33, No. 20 (1999), pp 1918-1938.

Y.J. Weitsman, "Effects of Fluids on Polymeric Composites-A Review," *Mechanical & Aerospace Engineering-Engineering Science*, report No. MAES-95-1.0/ADA297030/9 (July 1995).

## Appendix A: FRP-CMU Material Parameters

### Some Material Properties

Equations 1 through 3 (pp 7, 8, 9) outline the defining physical principles governing moisture migration through porous structures. However, the application of these principles to any particular system requires an accurate and detailed knowledge of the relevant individual physical parameters and their sensitivity to moisture and temperature. Generally, such data has not existed in traditional handbook format, and what data did exist was incomplete, unique to a given task or environment, and non-uniform.

Within the past 10 to 15 years, the building physics community has made a concerted effort to develop experimental techniques to evaluation of these functions and to compare predicted results with available field data. This effort has been predominately centered in Northern Europe and Canada, and is producing results to standardize and assemble all relevant data into a single set of documents. The culmination of this effort has been a series of documents, the most recent of which is Annex XXIV, Task 3 (Kumaran 1996). The Annex represents contributions from a number of member countries and reflects the diverse needs, interests, material properties, manufacturing and experimental methodology of individual members. Still, the Annex represents the best documented summary of unclassified, common building material hygro-thermal properties currently available to research groups.

### Concrete

A brief survey of the various concretes listed in the Annex clearly implies that the lighter concretes can absorb proportionally more moisture. A typical CMU found in the present study has a (dry) mass density of order  $2140 \text{ kg/m}^3$ , which is characteristic of a standard concrete. Drawing upon the listed Annex data, literature references (van Zijl 1999; Janz 1997), and standard engineering practice it is possible to deduce hygro-thermal material properties appropriate to this

density and having a global error of some 10 to 15 percent. Equations A1 through A3 express these data, with the moisture,  $\theta$ , measured in units of  $\text{kg}/\text{m}^3$ , relative humidity (RH) expressed a fraction, and an assumed (unless otherwise qualified) temperature of 20 °C:

**Concrete: Isothermal Absorption (wetting) Function (Kumaran 1996)**

$$\theta (\text{kg}/\text{m}^3) = ax^3 + bx^2 + cx + d \quad \text{Eq A1}$$

where:

$x$  is the relative humidity, expressed a fraction, and  
 $a = 26.68$   
 $b = -247.75$   
 $c = 123.45$   
 $d = 0.1076$ , for 2200  $\text{kg}/\text{m}^3$  concrete.

**Concrete: Isothermal, Desorption (drying) Function (Kumaran 1996)**

$$\theta (\text{kg}/\text{m}^3) = ax^4 + bx^3 + cx^2 + dx + e \quad \text{Eq A2}$$

where:

$x$  is the relative humidity, expressed a fraction and,  
 $a = 257.64$   
 $b = -426.95$   
 $c = 202.88$   
 $d = 77.823$   
 $e = -0.0104$ , for 2200  $\text{kg}/\text{m}^3$  concrete.

**Concrete: Wetting Moisture Diffusion Function,  $D_\theta$**

Concrete is a heterogeneous mix of sand, aggregate (gravel), water, and cement and is typically characterized by its mass density. Both the Annex and van Zijl (1999) list comparable values for  $D_\theta$ :

$$\log_{10} (D_\theta [\text{m}^2/\text{s}]) = 0.01942\theta - 10.5 \text{ (dimensionless)} \quad \text{Eq A3}$$

for:  $0.0 < \theta [\text{kg}/\text{m}^3] \leq 200$

**Concrete: Drying Moisture Diffusion Function,  $D_\theta$  (van Zijl 1999)**

$$\log_{10} (D_\theta [\text{m}^2/\text{s}]) = f(\theta) \text{ (dimensionless)}, \quad \text{Eq A4}$$

$$f(\theta) = a\theta^6 + b\theta^5 + c\theta^4 + d\theta^3 + e\theta^2 + f\theta + g$$

for:  $0.0 < \theta [\text{kg/m}^3] \leq 200$

where:

$$\begin{aligned}a &= 1.0108823 \text{ E-12} \\b &= -7.846242 \text{ E-10} \\c &= 2.4277506 \text{ E-7} \\d &= -3.7851524 \text{ E-5} \\e &= 3.071331 \text{ E-3} \\f &= -0.09861641 \\g &= -8.9905065\end{aligned}$$

### **Concrete: Thermal Moisture Diffusion Function, $D_T$**

The Annex (Kumaran 1996) lists a representation for the Thermal Moisture Diffusion Function,  $D_T$ . However a more common and useful alternative formulation is possible, based on the “WUFI-ORNL/IBP, Hygrothermal Design Tool for Architects and Engineers” format (Kuenzel et al. 2000). In this representation the thermal flux vector,  $D_T \nabla T$  of Equation 1 (p 7), and which describes the moisture *vapor* migration is replaced as follows:

$$D_T \nabla T [\text{kg/m}^2 \cdot \text{s}] = (\delta_P(T) / \mu) \nabla (h P_s(T)) \quad \text{Eq A5}$$

and

$$P_s(T) [\text{Pa}] = P_o \exp(-(\Delta H/R)[1/T - 1/373.15])$$

Here  $\mu$  is the (dimensionless) vapor resistivity, and is a physical parameter that provides a measure of moisture vapor transport through a material medium. The vapor resistivity can have some sensitivity to both humidity and temperature. For concrete with a typical density of order 2200  $\text{kg/m}^3$ , the Annex (Kumaran 1996) lists:

$$\begin{aligned}1/\mu &= [0.0068 + (8.21 \times 10^{-5}) \exp(5.66h)] \\ \Delta H/R &= 5201.08 [\text{°K}], \text{ measured for liquid water, and} \\ P_o &= 101,325 [\text{Pa}], \text{ the pressure of a standard atmosphere, also equal to 76 cm} \\ &\text{of Mercury.} \\ T &= \text{the absolute thermodynamic temperature, measured in degrees Kelvin,} \\ &\text{and} \\ h &= \text{the relative humidity (RH), expressed as a fraction.}\end{aligned}$$

The Annex lists a version of  $\delta_P(T)$ , however an equivalent representation is:

$$\delta_P(T) = 1.83 \times 10^{-10} (T / 273.15 \text{ °K})^{0.81} (P_o / P) [\text{kg/m.s.Pa}].$$

Here  $P$  represents the ambient atmospheric pressure, which is taken to be identical to  $P_o$  for this modeling effort.  $\delta_P(T)$  is then, the calculated value of the vapor permeability of water through air, evaluated at a standard atmosphere. At this time,  $\delta_P(T)$  is not known to have been experimentally determined for air.

In this representation of  $D_T \nabla T$ , the thermal flux vector is now seen to have both temperature and moisture sensitivity, through the  $hP_s(T)$  function. When operated upon by the  $\nabla$ , both  $h$  and  $T$  cross terms are generated containing the gradient of the complementary term. The  $P_s(T) \nabla (h)$  term will (or can be) combined with the  $D_\theta \nabla \theta$  term of Eq 1 (p 7), resulting in a weak thermal sensitivity.

### **Concrete Thermal Data**

The specific heat capacity of concrete,  $c$ , is known to have some temperature sensitivity, that is of order 3 to 4 percent for temperatures between 10 and 37 °C, and was derived for fully saturated normal-weight samples. A similar sensitivity may exist for unsaturated samples, however no data appear to exist to support this assumption (Van Geem and Fiorato 1983). Given this, the Annex list the thermal data as expressed in Equation A6.

#### **Concrete Volumetric Heat Capacity**

$$\rho c \text{ [J/m}^3 \cdot \text{°C}] = \rho_o c_o + 4187 \text{ [J/kg. °C]} \theta \quad \text{EqA6}$$

where:

$$\begin{aligned} \rho_o &= 2200 \text{ [kg/m}^3], \text{ dry material} \\ c_o &= 940 \text{ [J/kg. °C] of dry material} \\ \theta &= \text{moisture content in [kg/m}^3] \end{aligned}$$

#### **Thermal Conductivity of Moist Concrete**

$$k_T \text{ [Watts/m. °C]} = 2.74 + 0.0032\theta$$

### **Polymers-Epoxy and FRP**

Reliable data on polymers, with and without fibers, is even more tenuous than that of traditional building materials, and must be gleaned by hand from available journal literature. An Epoxy resin being considered for use in this study is EPON 828RS (Shell Chemicals), a liquid difunctional bisphenol A/epichlorohydrin-derived resin, of average molecular weight 378 grams/mol. The corresponding FRP is a Vinyl Ester-glass fiber composite, EXTREN®, for

which there exists moisture uptake as a function of ambient relative humidity. In either case, the relative permeability to moisture is small, roughly that of a Type-1 (polymer) vapor barrier, and some two orders of magnitude less permeable than a typical CMU.

### **Epoxy Resin: Moisture Data**

Some moisture data has been determined for Epoxy by direct immersion in several penetrant liquids of interest, including distilled water (Chin et al. 1999). No humidity data is available, and it is assumed that the vapor sensitivity is negligibly small in keeping with the previous remarks. From the data of (Chin et al. 1999), one can deduce the Arrhenius temperature dependence and activation energy,  $\Delta H$ , for both (assumed) wetting and drying moisture transport as follows:

$$D_\theta [\text{m}^2/\text{s}] = D_o \exp(-\Delta H/RT) \quad \text{Eq A7}$$

Note that:  $D_T$  [kg/m.s. °K] is unknown, and assumed = 0.0; see, FRP below.

Where:

- $\Delta H$  = 69742.97 [J/mol] for Epoxy, and
- $D_o$  = 0.11854 [m<sup>2</sup>/s], the diffusion coefficient in the reference state,
- $T$  = the absolute thermodynamic temperature, measured in degrees Kelvin.
- $R$  = 8.314 [J/mol. °K], the thermodynamic gas constant.

### **FRP and Vinyl Ester Resin: Moisture Data**

A limited amount of actual moisture diffusion data is available for the Vinyl Ester-glass fiber composite, EXTREN® (Verghese et al. 1999). Measurements were performed for relative humidities (RH) of 75, 85, and 100 percent water bath environments, with an assumed temperature of 60 °C. Based on the corresponding moisture saturation levels and an assumed matter density for a polymer (epoxy, FRP) of 1160 kg/m<sup>3</sup>, Verghese et al., assign the following functional relation between moisture density and relative humidity.

### **Matrix and FRP: Isothermal Absorption Function**

$$\theta [\text{kg/m}^3] = 7.53 (x)^{4.3} \quad \text{Eq A8}$$

Where:

- $x$  is the relative humidity (RH), expressed a fraction, and
- the drying function is *assumed* to be identical to the wetting function.

### **Matrix and FRP Moisture Diffusion (wetting/drying) Function, $D_\theta$**

Continuing with the results of Verghese et al. (1999) and Chin et al (1999), one can deduce (approximately) the Arrhenius temperature dependence and activation energy,  $\Delta H$ , and moisture functionality for both wetting and drying moisture transport as follows:

$$D_\theta [\text{m}^2/\text{s}] = (G(\theta)) [D_o \exp(-\Delta H/RT)]$$

Where:

$\Delta H$  = 21832.8 [J/mol] for Vinyl Ester (Chin et al. 1999), and  
 $D_o$  =  $\exp(+\Delta H/RT)$ , for  $T = (273 + 60)^\circ\text{K}$  (Hence,  $D_o = 2659.7$ , the dimensionless diffusion coefficient premultiplier in the reference state; here  $D_o$  is chosen so that  $D_\theta$  is consistent with Verghese et al. (1999), for  $T = 333^\circ\text{K}$ ).  
 $T$  = the absolute thermodynamic temperature, measured in degrees Kelvin.

The quality of the moisture sensitivity data is subject to errors, limitations of graphical transcription and measurement; as such, a simple linear fit is most appropriate to the data (Verghese et al. 1999).

$$G(\theta) = (a\theta + b) \times 10^{-13} (\text{m}^2/\text{s})$$

for:

$$0.0 < \theta [\text{kg}/\text{m}^3 \text{ of moisture}] \leq 10$$

Where:

$$\begin{aligned} a &= -1.865297 [\text{m}^3/\text{kg}] \\ b &= 49.124578 \end{aligned}$$

### **Matrix and FRP: Thermal Moisture Diffusion Function, $D_T$**

Actual FRP data for the thermal moisture diffusion function,  $D_T$ , does not appear to exist at this time. However adopting the same format as for concrete, based on the “WUFI-ORNL/IBP, Hygrothermal Design Tool for Architects and Engineers” formulation (Kuenzel et al. 2000), permits a bounding approximation.

$$D_T \nabla T [\text{kg}/\text{m}^2 \cdot \text{s}] = (\delta_p(T) / \mu) \nabla (h P_s(T)) \quad \text{Eq A10}$$

and

$$P_s(T) [\text{Pa}] = P_o \exp(-(\Delta H/R)[1/T - 1/373.15])$$

$\mu$  is the (dimensionless) vapor resistivity, and is a physical parameter that provides a measure of moisture vapor transport through a material medium. The vapor resistivity can have some sensitivity to both humidity and temperature, and is of order 40,000 for Epoxy resin (Kunzel 1995).  $\delta_P(T)$  and all other physical constants and parameters are as listed in Eq A5.

## Epoxy Polymer and FRP Thermal Data

The thermal conductivity of a widely used thermoset resin, Hercules 3501-6, has been measured over a wide temperature range (Chern et al. 1993). In the derivation, these authors assume that the volumetric heat capacity of the epoxy is comparable to that of a heating resistance wire, say copper. Assuming this and a typical matter density for a polymer (epoxy, FRP) of 1160 kg/m<sup>3</sup>, one then has the following thermal data:

### Epoxy Polymer Volumetric Heat Capacity

$$\rho_E c_E [\text{J/m}^3 \text{ }^\circ\text{C}] = \rho_o c_o + 4187 [\text{J/kg }^\circ\text{C}] \theta$$

where:

$$\rho_o c_o = 0.36 \times 10^7 [\text{J/m}^3 \text{ }^\circ\text{C}], \text{ dry material}$$

$$\theta = \text{moisture content in [kg/m}^3\text{].}$$

Thermal Conductivity of Host (Epoxy Polymer) Material (100% cured and assumed dry [Chern et al. 1993]):

$$k_T [\text{Watts/m }^\circ\text{K}] = aT^4 + bT^3 + cT^2 + dT + e \quad \text{Eq A11}$$

where:

$T$ =	the absolute thermodynamic temperature, measured in degrees Kelvin and,
$a$ =	-9.522 E-11
$b$ =	1.111 E-7
$c$ =	-4.057 E-5
$d$ =	4.263 E-3
$e$ =	0.382

## Matrix and FRP Thermal Data

The thermal conductivity and the volumetric heat capacity for the matrix and FRP composite are generalized functions of the individual epoxy and fiber glass constituents, the details of how the individual applique is put together and applied to the substrate. Given this and the general impracticality of in situ measurements, the next best approach is to approximate these thermal parameters following standard mixture techniques (Hashin 1968; Halpin 1984; Springer 1981).

### FRP Volumetric Heat Capacity

The use of mixture techniques to derive the volumetric heat capacity for the Matrix-Fiber combination gleans support from the fact that this thermal parameter is related to the global volume properties of the combined materials, in a simple additive way, that reflects the total thermal energy per unit volume. Thus the epoxy matrix-FRP volumetric heat capacity,  $\rho_{E-F}c_{E-F}$ , is:

$$\rho_{E-F}c_{E-F} [\text{J/m}^3 \cdot ^\circ\text{C}] = v_f \rho_X c_X + (1-v_f) \rho_E c_E \quad \text{Eq A12}$$

where:

- $\rho_{E-F}c_{E-F}$  = the total Epoxy Matrix-FRP volumetric heat capacity [J/m<sup>3</sup>.°C]
- $\rho_E c_E$  = the Epoxy volumetric heat capacity with moisture functionality from above
- $\rho_X c_X$  =  $\rho_{GI}c_{GI} = 0.209 \times 10^7$  [J/m<sup>3</sup>.°C], the dry volumetric heat capacity of glass fibers.

However, if carbon fibers are used, then

- $\rho_X c_X = \rho_C c_C = 0.128 \times 10^7$  [J/m<sup>3</sup>. °C], the dry volumetric heat capacity of carbon fibers, and  $v_f$  is the fiber volume fraction, around 0.60, for both cases.

### Thermal Conductivity of FRP Material

A particular complication for the Epoxy-FRP composite is the anisotropic nature of the thermal conductivity, which arises from the unidirectional fibrous nature of the FRP within the epoxy matrix. However, it has been suggested that the transport property of unidirectional composites along the longitudinal direction may be approximated using the standard rule of mixtures approach (Hashin 1968; Halpin 1984; Springer 1981), as follows.

$$k_L [\text{Watts} / \text{m} \cdot ^\circ\text{C}] = v_f k_f + (1-v_f) k_T \quad \text{Eq A13}$$

where:

- $k_L$  is the longitudinal thermal conductivity [Watts / m. °C]
- $v_f$  is the fiber volume fraction, around 0.60
- $k_f$  is the thermal conductivity of the fiber, 1.05 Watts / m. °C for glass and 80 Watts / m. °C for carbon in the longitudinal direction and 12.5 Watts / m. °C for carbon in the transverse direction
- $k_T$  is the thermal conductivity [W / m. °C] of the epoxy matrix from Equation A11.

The transverse thermal conductivity of a continuous fiber FRP,  $k_{Tran}$ , which is also the out-of-plane conductivity value, uses the Halpin-Tsai equation Agraal and Broutman (1990):

$$k_{Tran} / k_T = (1 + \eta v_f) / (1 - \eta v_f) \quad \text{Eq A14}$$

where:

$$\eta = [(k_f / k_T) - 1] / [(k_f / k_T) + 1] \quad \text{Eq A-15}$$

and

$k_f$ ,  $k_T$  and  $v_f$  are defined from above  
and it assumes that circular cross-sections exist in the fibers.

# REPORT DOCUMENTATION PAGE

Form Approved  
OMB No. 0704-0188

Public reporting burden for this collection of information is estimated to average 1 hour per response, including the time for reviewing instructions, searching existing data sources, gathering and maintaining the data needed, and completing and reviewing this collection of information. Send comments regarding this burden estimate or any other aspect of this collection of information, including suggestions for reducing this burden to Department of Defense, Washington Headquarters Services, Directorate for Information Operations and Reports (0704-0188), 1215 Jefferson Davis Highway, Suite 1204, Arlington, VA 22202-4302. Respondents should be aware that notwithstanding any other provision of law, no person shall be subject to any penalty for failing to comply with a collection of information if it does not display a currently valid OMB control number. PLEASE DO NOT RETURN YOUR FORM TO THE ABOVE ADDRESS.

1. REPORT DATE (DD-MM-YYYY) 09-2003			2. REPORT TYPE Final		3. DATES COVERED (From - To)	
4. TITLE AND SUBTITLE Hygrothermal Modeling in the Application of Fiber-Reinforced Polymers for Structural Upgrade of Unreinforced Masonry Walls					5a. CONTRACT NUMBER	
					5b. GRANT NUMBER	
					5c. PROGRAM ELEMENT NUMBER	
6. AUTHOR(S) Carl A. Feickert, Mark W. Lin, Jonathan C. Trovillion, Ayo O. Abatan, and Justin B. Berman					5d. PROJECT NUMBER 611102AT23	
					5e. TASK NUMBER	
					5f. WORK UNIT NUMBER 007AV5	
7. PERFORMING ORGANIZATION NAME(S) AND ADDRESS(ES) U.S. Army Engineer Research and Development Center (ERDC) Construction Engineering Research Laboratory (CERL) PO Box 9005 Champaign, IL 61826-9005					8. PERFORMING ORGANIZATION REPORT NUMBER ERDC/CERL TR-03-20	
9. SPONSORING / MONITORING AGENCY NAME(S) AND ADDRESS(ES) U.S. Army Engineer Research and Development Center (ERDC) Construction Engineering Research Laboratory (CERL) PO Box 9005 Champaign, IL 61826-9005					10. SPONSOR/MONITOR'S ACRONYM(S) CEERD-CV-ZT	
					11. SPONSOR/MONITOR'S REPORT NUMBER(S)	
12. DISTRIBUTION / AVAILABILITY STATEMENT Approved for public release; distribution is unlimited.						
13. SUPPLEMENTARY NOTES Copies are available from the National Technical Information Service, 5285 Port Royal Road, Springfield, VA 22161.						
14. ABSTRACT The Army maintains an aging inventory of over 143,000 structures, many of which are in urgent need of maintenance and repair. In some instances, these aging structures fail to meet prevailing seismic engineering codes. In the United States alone, 30 percent of the Army's structures use unreinforced masonry (URM) walls. As such, URM structures have inadequate plane lateral strength and are prone to failure during seismic events. Upgrading these structures to meet existing seismic codes often requires the use of new materials and systems such as fiber-reinforced-polymer (FRP) composites. The versatility and resilience of such advanced composites make them ideal candidate materials for reducing the cost of seismic rehabilitation of DOD facilities. Though many studies have demonstrated the effectiveness of FRP reinforcements as structural upgrades for masonry walls, little has been done to explain their impact on the building envelope. This study was undertaken to discover and define the combination of building envelope and hygrothermal conditions that might result in vapor liquefaction at the ceramic-epoxy interface, and subsequently debond or delaminate the applique. This research developed fundamental models and associated material parameters to predict thermal and moisture transport across dissimilar building materials—specifically FRP composite appliques to concrete masonry units (CMUs)—used for seismic upgrades.						
15. SUBJECT TERMS fiber-reinforced polymer (FRP)      composite materials      computer simulation masonry      building materials      modeling						
16. SECURITY CLASSIFICATION OF:			17. LIMITATION OF ABSTRACT SAR	18. NUMBER OF PAGES 68	19a. NAME OF RESPONSIBLE PERSON Carl A. Feickert	
a. REPORT Unclassified					b. ABSTRACT Unclassified	
					19b. TELEPHONE NUMBER (include area code) (217) 352-6511, X-7473	